Compaction-mediated segregation of partly replicated bacterial chromosome

Sumitabha Brahmachari,[1,*] Antonio B. Oliveira Jr.,[1] Matheus F. Mello,[1] Vinícius G. Contessoto,[1] and José N. Onuchic[1,2,3,4]

[1] *Center for Theoretical Biological Physics, Rice University, Houston, TX 77005, USA*
[2] *Department of Biosciences, Rice University, Houston, TX 77005, USA*
[3] *Department of Physics and Astronomy, Rice University, Houston, TX 77005, USA*
[4] *Department of Chemistry, Rice University, Houston, TX 77005, USA*

Bacterial chromosome segregation, ensuring equal distribution of replicated DNA, is crucial for cell division. During fast growth, replication and segregation co-occur. Overlapping cycles of DNA replication and segregation require efficient segregation of the origin of replication (Ori), which is known to be orchestrated by the protein families SMC and ParAB. We used data-driven physical modeling to study the roles of these proteins in Ori segregation. Developing a polymer model of the Bacillus subtilis genome based on Hi-C data, we analyzed chromosome structures in wild-type cells and mutants lacking SMC or ParAB. Wild-type chromosomes showed clear Ori segregation, while the mutants lacked faithful segregation. The model suggests that the dual role of ParB proteins, loading SMCs near the Ori and interacting with ParA, is crucial for Ori segregation. ParB-loaded SMCs compact individual Ori and introduce an effective inter-sister repulsion that regulates the ParAB-activity to avoid the detrimental scenario of pulling both Ori to the same pole. The model makes testable predictions for sister-chromosome-resolved Hi-C experiments and proposes that replicated sister chromosomes segregate via mechanistic cooperation of SMC and ParAB activity.

Introduction. Segregation of replicated DNA or sister chromosomes is crucial for equally dividing the duplicated genetic material during cell division. In exponentially growing bacteria, DNA replication and segregation are known to co-occur. The early-replicated sister chromosomes get positioned at opposite poles of the bacterial cell while the rest of the DNA undergoes replication [1, 2]. The polar segregation of early-replicated DNA guides the physical separation of fully duplicated sister chromosomes required for cell division. The activity of proteins in the SMC (Structural Maintenance of Chromosome) family and the ParAB system are the primary drivers of this segregation; however, the underlying mechanism is poorly understood [1–3]. Using data-driven physical modeling of the chromosome structure, we investigate the mechanistic interplay of these proteins in segregating the partly replicated chromosomes.

Bacterial chromosomes are typically circular and have one origin of replication (Ori), where the DNA replication apparatus or the replisome is assembled. Two replisomes then proceed in opposite directions from the Ori, resulting in two DNA replication forks proceeding along the two chromosome arms, which meet at the end or terminus (Ter) of the chromosome (Fig. 1A). A successful cell division requires the replicated sister chromosomes to physically segregate and occupy opposite poles of the rod-shaped bacteria before a contractile ring drives the cell septum. Under fast growth conditions, new rounds of replication initiate before completing the previous one [2]. To ensure that DNA is segregated in the same order as they are replicated, the newly replicated Ori regions are pulled apart to occupy opposite poles before the replication round is finished [2, 3]. Mutant cells lacking either SMC or ParAB activity are known to lack early Ori segregation [4–7]. We are interested in the underlying mechanism: are these proteins acting independently or cooperating to segregate the newly-replicated Ori?

The ParAB system comprises ParA, an ATPase that dimerizes in the presence of ATP, and ParB, a DNA-binding protein that strongly prefers binding specific centromere-like DNA sequences, called parS [3]. The parS sequences typically cluster around the origin of replication in bacteria [8]. Encountering parS-bound ParB stimulates the ATPase activity of ParA-ATP dimers, resulting in ParA monomerization and a local depletion of ParA-ATP dimers. This mechanism allows the ParB/parS complexes to move along the ParA-ATP dimer gradient [9, 10]. Bacterial cell poles have higher concentrations of ParA [9, 11, 12], effectively generating poleward forces that can pull the Ori-proximal ParB-bound DNA. Importantly, the sequence-similarity of the replicated Ori pair suggests this force should act equally on both the Ori. How, then, are the two Ori pulled to opposite poles?

We hypothesize that this conundrum is resolved by a dual role of ParB proteins. On one hand, ParB acts as a loader of loop-extruding SMC proteins, such that SMCs are enriched near each Ori [5, 13–18]. SMC/ParB-driven Ori lengthwise compaction will introduce repulsion between the replicated Ori. On the other hand, ParB-bound Ori-proximal DNA experiences a poleward pulling force due to the presence of ParA, as described above. While the ParAB-driven force pulls one of the Ori towards its nearest pole, the SMC/ParB-driven force will push the other Ori towards the opposite pole. This mechanism predicts efficient polar segregation of Ori only by combining the activities of ParAB and SMC, and a depletion of either will suppress polar segregation.

* sb95@rice.edu

Model. To quantitatively test this hypothesis, we built polymer models of the genome of rod-shaped bacterium *Bacillus subtilis* (*B. subtilis*) by combining a data-driven approach with phenomenological modeling (Fig. 1). We derived structural ensembles of the *B. subtilis* chromosome confined within the cylindrical cell that are quantitatively consistent with the experimental pairwise-contact information from Hi-C data (Fig. 1B) [14]. The ParAB activity is phenomenologically modeled as a double-well potential with minima near the poles of the cylinder (Fig. 1C). The minima are symmetric and shallow (1 k_BT) to make transitions accessible by thermal fluctuations. It is important to note that this potential only acts on the eight Ori-proximal monomers containing the parS sites (see Supplementary).

Our data-driven-polymer scheme based on entropy maximization optimizes an effective pairwise potential within the constraints of experimental Hi-C data (Fig. 1 C-F and Supplementary text) [19]. The data-driven potential offers the most general formulation under the constraints of chromosomes' polymeric nature, cellular confinement, and the experimentally observed contact probability of loci pairs. We learn the effective polymer potential of a non-replicating chromosome for the Wild-type (WT) and mutants with SMC depletion (ΔSMC) and ParAB depletion (ΔParAB) from experimental data [14] (Figs. S1, S2, S3). The learned potential is then used to generate polymer trajectories that furnish structural ensembles and the effective structural dynamics associated with each phenotype. The model for a non-replicating *B. subtilis* chromosome comprises a circular polymer of 404 monomers, where each monomer of size $\sigma = 80$ nm contains 10 kb DNA. The cylindrical confinement mimicking the bacterial cell wall has a diameter of 6σ or about 0.5 μm, and an axial length of 16σ or 1.3 μm. The Hi-C-derived structural ensembles are in quantitative accord with imaging experiments, providing independent validation (Fig. 1G-H).

Results. *B. subtilis* Hi-C maps show an enriched diagonal due to the polymer chain being locally crumpled or lengthwise compacted (Fig. 1C-E) [14]. The circular nature of the chromosome polymer enhances the farthest corner of the map away from the diagonal. The WT ensemble is characterized by a pairing of the two chromosome arms such that loci pair genomically equidistant from the Ori are in spatial proximity. The pairing results in an additional anti-diagonal ("X"-shaped) Hi-C pattern in WT when the Ori is placed at the center of the map (Fig. 1D). The mutant phenotypes lack this feature (Fig. 1E, F). Although our approach is agnostic of the underlying mechanisms, elegant experiments put forward strong evidence that ParB-mediated loading of SMCs near the parS-enriched Ori coupled with the processive extrusion activity of SMCs drive the pairing of arms [15, 17, 18].

A crucial difference between the WT and mutant ensembles is the cis-compaction of Ori-proximal DNA (Figs. 1D-F, S4A). Enhanced WT Ori compaction has been attributed to a high density of ParB-loaded SMCs trapped in a jammed state [15, 17, 18]. We propose this ParB/SMC-driven compaction is a driver of the observed Ori segregation. ΔParAB mutant exhibits territorial chromosome arms characterized by enhanced intra-arm interactions (Fig. 1E).

Interestingly, the SMC mutant shows a significantly stronger Hi-C diagonal, suggesting an enhanced lengthwise compaction (Fig. 1F). This lengthwise compaction is not from loop extrusion; instead, transcription is the likely driver. Supercoiled DNA plectonemes introduced by transcription can effectively increase the short-range cis-interactions [20, 21]. This predicts a critical role of SMCs in managing the transcription-induced plectoneme organization. The interplay of SMC activity and DNA supercoiling has garnered interest in recent years [22, 23]. Future experiments are needed to investigate if plectonemes are the source of short-range intra-arm compaction in SMC mutants.

The Ori shows a polar localization in WT and ΔSMC phenotypes due to the polar ParAB force, originating from the double-well potential, acting on the parS-containing monomers (Figs. 1C, D, F, and S4). This potential is absent in ParAB mutants (ΔParAB), resulting in a mid-cell localization of Ori (Figs. 1E, and S4). The ΔParAB ensemble shows a "left arm-Ori-right arm" configuration, resembling vegetatively growing *B. subtilis* cells [1] (Fig. 1E).

The next step is to construct the effective potential of a replicating chromosome using the data-driven single chromosome potential (Fig. 2A). The geometry of the replicating chromosome is such that two sister chromosomes are connected with the unreplicated region at the two fork positions or replisomes (Fig. 2B). Since Hi-C cannot distinguish between the genomically identical sister chromosomes, we assumed that the learned single chromosome potential is for a non-replicating chromosome (Fig. 1B-F).

We argued that since the sister chromosomes have identical DNA sequences, the interaction potential for the two sisters is symmetric. The interactions between the sisters and those between a sister and the unreplicated region are modeled the same way as in the non-replicating case (Fig. 2A-B). The symmetrization scheme allowed us to assign data-driven potentials between all the loci pairs of the replicating chromosome except the inter-sister interactions. As a simplification, we assumed a uniform, non-specific interaction between the newly replicated sisters. While the diagonal and the anti-diagonal regions of the WT Hi-C map harbor contacts driven by, respectively, the polymer connectivity and SMC/ParB activity, the remaining region, capturing Ori-Ter contacts, represents the baseline for non-specific interactions (Fig. S5). This non-specific baseline potential in the non-replicating case is used for the uniform inter-sister interactions (Fig. 2A).

The replicating chromosomes are then simulated in a confined cylinder with the ParAB potential (Fig. 2C). The ParAB poleward force will drive each Ori to the near-

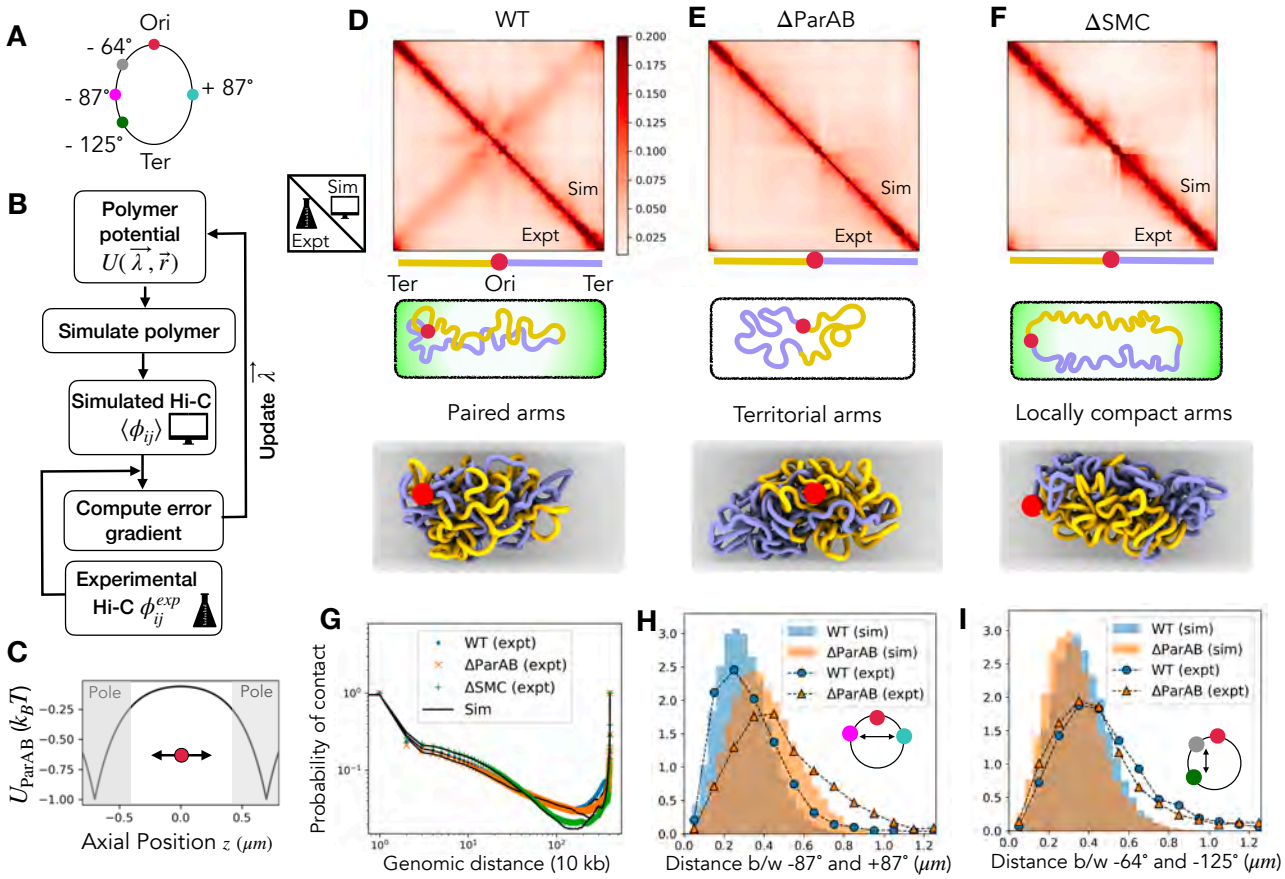

FIG. 1. **Inferring structural ensembles from Hi-C data.** (A) Circular bacteria chromosome showing the origin (Ori) and terminus (Ter) of replication. Loci on the left and right arms are denoted using negative and positive degrees. (B) Entropy maximization scheme for iteratively optimizing the effective potential of a circular polymer, such that the polymer configurations are consistent with Hi-C contacts. (C) The phenomenological ParAB potential is radially uniform and varies only along the axial length of the cylindrical confinement with two minima near the poles of the cell. This potential only applies to the Ori-proximal parS-containing monomers when ParAB is present. (D) Comparison of the WT simulated contact map (upper triangle) with the experimental *B. subtilis* Hi-C map (lower triangle) [14]. The Ori is centrally positioned, which gives rise to the strong anti-diagonal depicting pairing of the chromosome arms in WT. A sketch of the typical chromosome conformation is shown below followed by a simulation snapshot. The two arms of the chromosome are shown in different colors; the Ori is shown as a red sphere. The green color at the poles represents ParAB activity. The cell wall is shown as a gray surface in the simulation snapshot. (E) Same as (D) for the ParAB mutant (ΔParAB). The chromosome conformations show territorial arms instead of pairing. Note the absence of the ParAB potential. (F) Same as (D) for SMC mutant (ΔSMC). The chromosome arms are locally compacted making them stiffer. (G) The scaling of the average probability of pairwise contact with genomic distance, comparing simulation with experiments [14]. Note the increased contact probability at very long distances, which is due to circular chromosomes. (H) Comparison of distances observed in imaging experiments [14] with the simulated ensembles for WT and ParAB mutant between the loci pair $-87°$ and $+87°$. The pairing of chromosome arms drives the higher proximity of these loci in the WT ensemble. (I) Same as in (H) for the loci pair $-64°$ and $-125°$.

est pole but does not ensure the two Ori occupy distinct poles, a configuration necessary for polar Ori segregation. We constructed the potential at various stages of replication, where each stage has a different size of the replicated sister chromosome. We denote ρ as the fraction of chromosome that is replicated (Fig. 2B). Assuming replication is slow compared to the polymer relaxation time, we used dynamic simulations with the constructed potential to obtain a distinct ensemble of chromosome conformations for various replicated fractions. This allowed us to predict the sister-chromosome resolved Hi-C maps at various replication stages (Fig. 2D-F shows the mid-replication stage for WT and mutants).

To measure the degree of Ori segregation in the structural ensembles, we used three indicators: the ratio of inter- to intra-sister contact probabilities, the topological entanglement or catenation of sister chromosomes, and the average distance between the two Ori-proximal regions (Fig. 3A-C). Our polymer ensembles feature topology fluctuations since there is only soft repulsion between

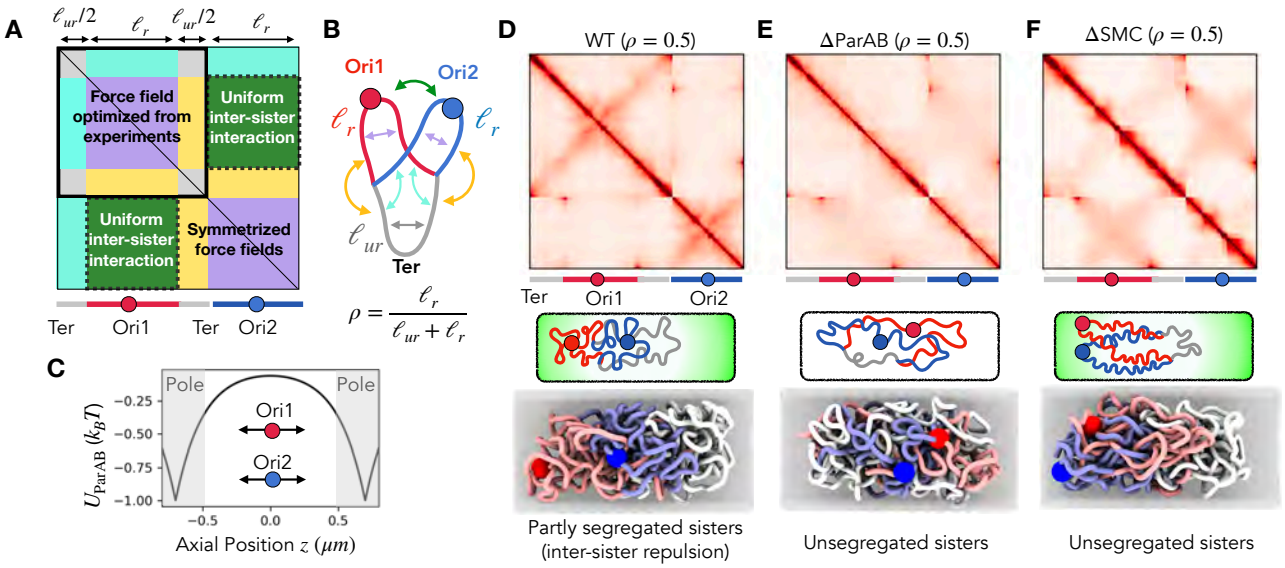

FIG. 2. **Effective potential for a partially replicated** *B. subtilis* **chromosome.** (A) The symmetrization scheme is used to construct the potential for a partially replicated bacterial chromosome from the non-replicating-chromosome data-driven potential shown in Fig. 1. The inter-sister part of the potential is assumed uniform and equal to the average non-specific interaction component in the data-driven potential ($U_{\mathrm{inter-sis}} = -0.18\ k_BT$, see Fig. S5). (B) Sketch of the partly replicated chromosome with two Ori. The interactions are shown by colored arrows where the color corresponds to specific blocks in the constructed potential shown in (A). The replication fraction ρ is defined as the ratio of replicated (ℓ_r) to total DNA length ($\ell_r + \ell_{ur}$). (C) The external double-well potential representing ParAB activity. This potential only acts on the Ori-proximal monomers containing parS sequences in both sister chromosomes and vanishes for the ΔParAB ensemble. (D) Simulated contact maps obtained from the simulation ensemble with $\rho = 0.5$, i.e., half of the chromosome is replicated, using the potential constructed following the symmetrization scheme. A sketch with the organization of the two Ori is shown below, followed by a simulation snapshot. The two replicated sister chromosomes are shown in red and blue colors, while the unreplicated part is shown in white. The two Ori are shown as red and blue spheres. The green color in the sketch depicts ParAB potential, and the gray surface in the snapshot is the cylindrical confinement. The same for the ΔParAB ensemble is shown in (E), and for the ΔSMC ensemble is shown in (F). Note the enhanced inter-sister contacts in the mutant ensembles even though there is a uniform intensity of trans-sister interaction in all three cases.

non-neighboring monomers. These topology fluctuations make the inter-sister catenation distribution unimodal and symmetric about zero (Fig. S6). The width or standard deviation of the inter-sister catenation distribution is used as a metric of inter-sister entanglement.

For low replicated fractions, the WT and both mutant ensembles show enhanced proximity of the two Ori that are entangled with a higher proportion of inter-sister contacts (Fig. 3A-C). In early replication stages, the two Ori occupy the same pole in WT and ΔSMC ensembles, while, in ΔParAB lacking poleward pulling, the Ori pair resides mid-cell (Figs. 3E-H, S4). During the mid-to-late replication stages ($\rho > 0.5$), the two WT Ori move away from each other, and there is a significant decay in the inter-sister contact and entanglements, suggesting Ori segregation (Fig. 3A-C). The average WT inter-Ori distance increases monotonically with replication fraction and saturates for higher values, signifying the two Ori occupying opposite poles (Fig. 3C) [24]. The mutants lack this crucial feature. The WT inter-sister distance is bimodal in mid-replication where the larger distance mode represents segregated Ori (Fig. 3D). The fraction of WT structures with segregated Ori increases with increasing replication fraction. The inter-sister distance in mutant ensembles remains unimodal at all replication stages, indicating a lack of Ori segregation (Fig. 3D).

The mid-cell-situated Ori pair in early replication shows enhanced dynamics in ΔParAB (Fig. 3G). Meanwhile, the Ori pair is less dynamic in the WT and ΔSMC ensembles as they are trapped at a pole due to the ParAB potential (Fig. 3F, H). In mid-replication, the WT Ori pair shows transitions between a bipolar segregated and a monopolar unsegregated state (Fig. 3F). The ΔSMC ensemble is predominated by the monopolar unsegregated configuration of the Ori pair (Fig. 3H). The ΔSMC Ori pair makes unsuccessful attempts to segregate with dampened dynamics (Fig. 3H). The sluggish dynamics is likely due to the locally compact arms of the ΔSMC chromosomes. Using Hidden Markov modeling, we estimated the residence times of the polar-Ori state to be lowest for the ΔParAB ensemble and highest for ΔSMC ensemble (Fig. 3I, S7). Calibrating simulation time with physical units: $\tau \approx 0.1$ sec (Supplementary text), suggests the Ori transitions out of the polar state occur approxi-

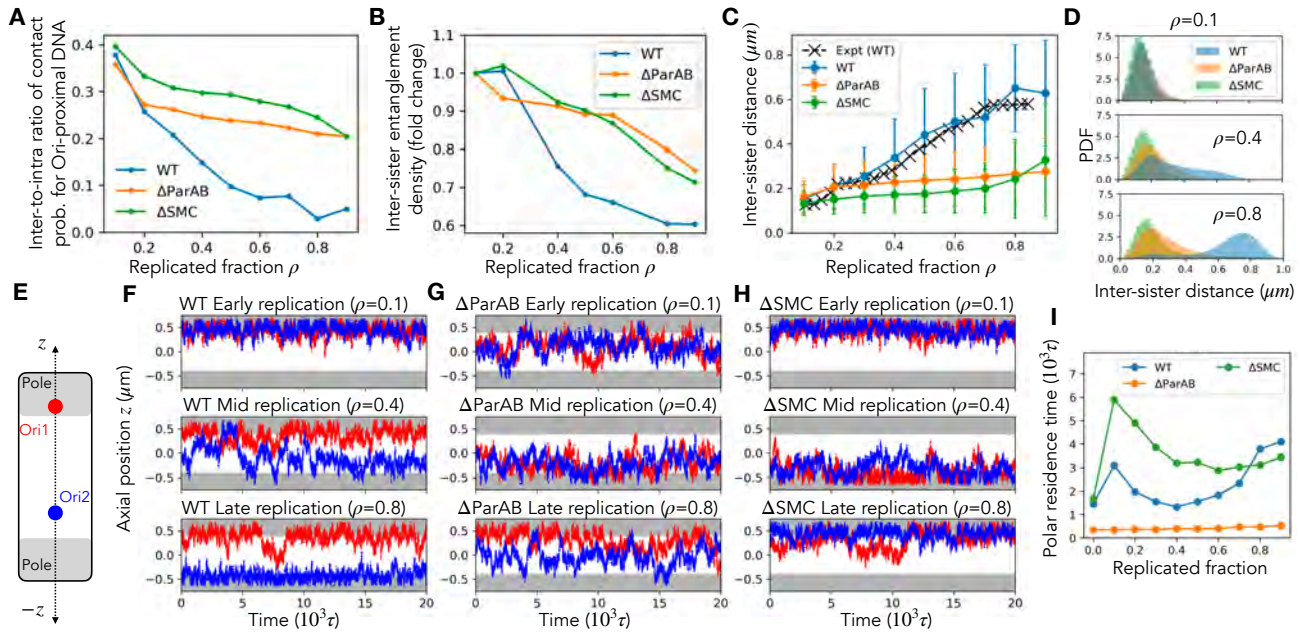

FIG. 3. **Analysis of structural ensembles shows Ori segregation deficiency in mutants.** (A) Ratio of average trans (inter) to cis (intra) contact probability between the Ori-proximal regions of the two sisters for various replication fractions. There is a strong depletion of inter-sister contacts for the higher replicated fractions in the Wt ensemble, suggesting a physically segregated Ori-pair in WT that is lacking in the mutants. (B) Inter-sister entanglement density, or inter-sister catenation per unit length (Fig. S6), for various replicated fractions, plotted as a fold-change over the early replication stage ($\rho = 0.1$). The catenations between the sisters are lower for higher replication fractions because of increased physical segregation between the sisters at later replication stages. (C) Distance between the two centers-of-masses of a 400 kb region (40 monomers) centered around the Ori of the two sisters for various replicated fractions. The WT ensemble shows the two Ori moving farther apart to opposite poles during the mid-replication stages. Meanwhile, the mutant ensembles show low inter-sister distance, indicating a lack of physical segregation between the replicated Ori. The black cross-marks are experimental data for *B. subtilis* [24], where a cell-doubling time of 40 minutes was used to convert time to a replicated fraction. (D) Probability distributions of inter-sister distances in early ($\rho = 0.1$), mid ($\rho = 0.4$), and late ($\rho = 0.8$) replication stages for the WT and mutant ensembles. The WT ensemble shows a bimodality at mid-replication stages corresponding to a mixture of configurations, where the small-distance peak corresponds to the two unsegregated Ori occupying the same pole, and the large-distance peak corresponds to the two segregated Ori distinct poles. The large-distance peak dominates in late replication stages, indicating a predominance of the segregated Ori configurations in WT ensembles. The mutants only show a small-distance peak, indicating an unsegregated Ori configuration during all the stages of replication. (E) Schematic of the bacterial cell with the cylindrical axis along the z direction. The polar positions are shaded in gray, and the two Ori are shown as red and blue circles. (F) Axial dynamics of the two WT Ori are shown in blue and red. The y axis depicts the polar coordinate in μm, and the x axis is the simulation time $\tau \approx 0.1$ sec (See Supplementary text and Fig. S11). The top panel corresponds to early replication ($\rho = 0.1$), the middle panel to mid-replication ($\rho = 0.4$), and the bottom panel to late-replication ($\rho = 0.8$). The two Ori are unsegregated in early replication, top panel ($\rho = 0.1$). In mid-replication (middle panel, $\rho = 0.4$), the WT Ori pair shows segregation attempts. By late replication (bottom panel, $\rho = 0.8$), the two Ori stably occupy opposite poles. The Ori dynamics across the replication stages for ΔParAB mutant is shown in (G), and the ΔSMC mutant is shown in (H). (I) The residence time for an Ori in the polar state, computed using Hidden Markov modeling (Fig. S7). The polar state is not stable in ΔParAB mutant due to an absence of the ParAB potential. The ΔSMC mutant shows increased stability of the polar state due to dampened dynamics resulting from the stiff chromosome arms. The slow dynamic of ΔSMC impedes the sergegation attempts of the Ori in the mid and late replication stages.

mately once every few minutes. WT cell division occurs roughly every 40 minutes, and the polar Ori segregation occurs over about 10 minutes [11, 17, 25]. Hence, these transitions offer a viable mechanism for Ori segregation in the mid-late replication stages. However, note that the dynamics is a characteristic of the effective potential constraining the structure, and this model does not have explicit motorized dynamics [26]. Motor-driven forces may drive these processes at a faster time scale. Late replication, the ΔParAB Ori pair continues to show enhanced mid-cell dynamics albeit with a slightly higher inter-Ori distance (Fig. 3C, D, and G). The WT ensemble exhibits bipolar segregated, stable Ori (Fig. 3F). Whereas, the ΔSMC dynamics continues unsuccessful attempts to segregate the Ori pair (Fig. 3H).

The underlying mechanism of Ori segregation combines inter-sister repulsion from ParB/SMC-mediated cis-compaction with the poleward Ori pulling by ParAB

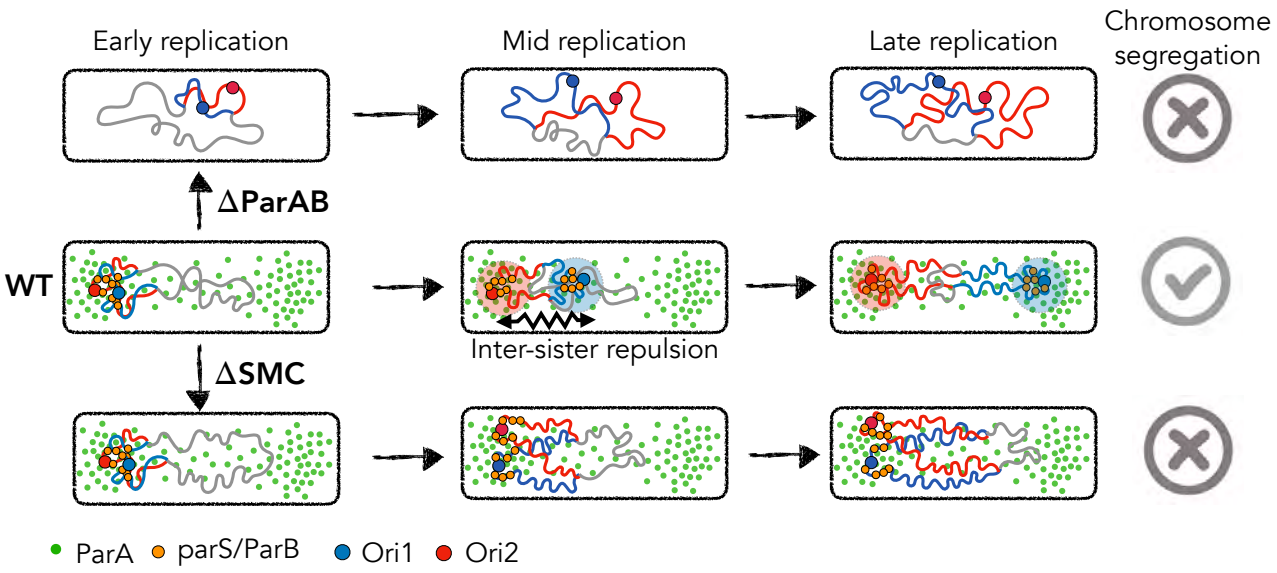

FIG. 4. **Compaction-mediated Ori segregation by SMC and ParAB.** In the early replication stages, the replicated Ori pair (shown as red and blue circles) remains nearby. The small green circles, depicting the ParA-ATP dimers, are enriched near the poles and depleted at the middle of the cell for WT and ΔSMC. While the ΔParAB ensemble lacks ParA (green circles) and ParB (orange circles) proteins. The parS/ParB complex can track the ParA-ATP gradient and facilitate their movement to the opposite poles. However, for this polar segregation, one (and not both) of the Ori must move away from the pole containing the unsegregated Ori pair. As more DNA is replicated in WT cells, SMC loading near the Ori by parS-bound ParB compacts the Ori-proximal DNA, introducing an effective inter-sister repulsion. The source of this repulsion in WT is the enriched cis contacts over trans contacts. The emergent inter-sister repulsion pushes one of the Ori away from the pole occupied by the other Ori. This results in the parS/ParB complex falling under the ParAB-driven attractive forces of the other pole, eventually leading to polar segregation of the Ori and the entire chromosome. The ΔParAB chromosome structure is not amenable to polar segregation of Ori since both the poleward forces and the Ori-specific loading of SMCs driving inter-Ori repulsion are missing. The chromosome structures for ΔSMC lack Ori-proximal compaction and stiff arms, leading to dampened dynamics. The lack of repulsion and slow dynamics result in severe segregation deficiency even in the presence of ParAB. This mechanistic cooperation between inter-sister repulsion and polar forces explains why the simultaneous activity of SMC and ParAB system is necessary for faithful polar Ori segregation during the mid-replication stages of the bacterial cell cycle.

(Fig. 4). The dominance of pairwise intra-sister contacts over the inter-sister ones in WT, due to ParB-mediated Ori-proximal loading of SMCs, introduces an effective inter-sister repulsion that increases with advancing replication. A similar mechanism based on the predominance of intra-contacts has been argued to establish strong chromosome territories, control inter-chromosome entanglements, and drive inter-sister segregation in mammalian chromosomes [27–29].

In early replication, the repulsion is weak, and both the Ori populate the same minimum (pole) of the ParAB potential (Fig. 4). Mid-replication, an increased repulsion between the replicated sisters promotes WT Ori's attempts to escape the occupied pole and approach the unoccupied pole, driving a segregated state. During this stage, the WT Ori pair show transitions between the segregated and the unsegregated states. By late replication, these transitions cease, and the two WT Ori settle in a bipolar, segregated state. The segregated state is not favored for the mutants. The missing ingredient is the ParB/SMC-driven inter-Ori repulsion that promotes segregation dynamics in the mid-replication stages. ΔParAB mutant possesses SMC complexes but lacks their Ori-proximal loading and the ParAB-mediated Ori pulling. While ΔSMC mutant lacks SMC-mediated lengthwise compaction of Ori, albeit it exhibits locally compact, stiff arms that inhibit segregation dynamics. Failure to possess either the ParAB poleward Ori pulling force or Ori compaction by SMC/ParB suppresses mid-replication Ori segregation and results in aberrant chromosome segregation (Fig. 4).

The simulated ensembles showed distinct positioning and dynamics of the replisomes in WT and mutants. The replisomes exhibit the highest physical proximity in the WT ensemble, while the ΔParAB mutant shows the farthest inter-replisome distance (Fig. S8A). In the WT ensemble, the replisomes are near the Ori-occupied pole in early replication; then, they move mid-cell during mid-replication stages and remain there till the end of replication (Fig. S8B). On the contrary, ΔParAB mutants show mid-cell localized replisomes during early replication, that move towards the poles in later stages of replication. Interestingly, ΔSMC mutants show the replisomes localized near the poles in early replication that

move to mid-cell in mid-replication and then revert back towards the poles in late-replication stages (Fig. S8B). The late-replication positioning is governed by the polar localization of the Ter region (Fig. S4). Imaging experiments have observed the close proximity of WT bacterial replisomes and their relocation from a polar to a mid-cell position with replication cycle progression [30].

Discussion. The predicted WT steady-state transitions between the segregated and unsegregated states in the mid-replication stages result from the symmetric ParAB potential with shallow minima (Figs. 2C, 3E). While the forward transition from an unsegregated to a segregated state has been observed experimentally [24, 31], the backward transition remains unverified. Introducing an asymmetry in the ParAB potential during mid-late replication, i.e., making one minimum deeper than the other, can exponentially suppress the backward rate and impart directionality to the segregation process. Imaging experiments suggest that the ParA concentrations at the two poles are indeed asymmetric [9, 12]. However, the discussed mechanism of Ori segregation via inter-Ori repulsion will still be relevant for the asymmetric potential.

Topology fluctuations are necessary for the proposed segregation process, i.e., the chain segments must be able to pass through each other to observe the reconfiguration dynamics. In vivo, topology fluctuations are controlled by DNA topoisomerase enzymes, and the presence of these enzymes is crucial for segregation [32]. Within our model, a short-range soft repulsion between all the monomers allows topology fluctuations while maintaining the volume exclusion aspects of DNA (Fig. S10).

ParAB-driven Ori movement from one pole to another has been proposed to work through a DNA-relay mechanism [9]. The DNA-relay model suggests that the tracking of ParA-ATP dimer gradient by parS-bound ParB, leading to an effective poleward force for the parS/ParB complex, is enhanced by polymer fluctuations. Our model possesses thermal fluctuations and argues that the poleward force only facilitates the movement of the Ori towards a pole and is insufficient to ensure bipolar segregation of replicated Ori. An interplay of SMC/ParB with the ParAB activity is essential for Ori segregation.

The model predictions do not break the segregation symmetry, i.e., which Ori goes to which pole is random. However, in *C. cresentus*, this symmetry appears to be broken [31]. The new Ori moves to the pole with a tail, while the old Ori sits at the original pole featuring a stalk. This poses interesting questions, yet unanswered, regarding the mechanism to recognize the new Ori and selectively pull it to the opposite pole. Possible hypotheses might involve aspects of asymmetry in the DNA replication process [33] or epigenetic mechanisms [34] or a combination of them.

Segregation of the parS/ParB complex to the opposite poles may contribute to bacterial plasmid partitioning. New evidence reports a tendency of ParB complexes to phase segregate [35], indicating an adhesive interaction between the ParB molecules. Many low-copy number plasmids are known to harbor the par locus [3]. This suggests the Ori-proximal DNA blob containing parS-bound ParB can also contain parS-featuring plasmids. Thus, Ori segregation will lead to a stochastic division between the plasmids stuck to each Ori-proximal DNA.

The entropic degrees of freedom of a random self-avoiding polymer have been previously proposed to drive the segregation of bacterial chromosomes [36]. Our homopolymer model, obtained by turning off the data-driven part of the potential, also showed sister-chromosome segregation but lacked many features of the experiments well-captured by the data-driven part (Fig. S9). This is because random polymer conformations are not representative of bacterial chromosomes.

Our solution to the problem of bacterial chromosome structure combines a data-driven maximum-entropy approach with dynamic polymer simulations that contrast 3D reconstruction approaches that fit structures to Hi-C maps and lack dynamics [37, 38]. Our approach also improves upon previous models utilizing the maximum-entropy potentials that relied on averaging interactions or truncating the less-probable long-range contacts for computational feasibility [39, 40].

Polymer modeling with explicitly loop extrusion has helped understand the role of SMC and ParB in driving the qualitative features of *B. subtilis* chromosome structure [17, 41]. Harju et al. [41] show that ParB/SMC activity may drive Ori segregation in WT. However, the study suggests this activity complements a self-sufficient mechanism of ParAB-driven segregation [41]. Notably, our model does not derive from apriori molecular mechanisms responsible for the 3D structure, such as loop extrusion. While our work agrees with the role of ParB/SMC, the results contrastingly suggest that the cooperation between ParAB and SMC/ParB activities is critical for the faithful segregation of the replicated Ori (Fig. 4). The lack of this cooperation diminishes the fidelity of Ori segregation in the SMC mutant (ΔSMC) [4–6].

Another data-driven model of bacterium *Escherichia coli*, which recapitulates various experimental features, also shows sister-chromosome segregation but lacks mechanistic insights [42]. The enrichment of the SMC-homolog MukBEF near the Ori, regulated by MatP [43, 44], controls the cellular positioning of the Ori [45]. Our results are consistent with a mechanism where the MukBEF-mediated Ori compaction introduces inter-Ori repulsion and drives mid-replication Ori segregation in *E. coli*.

We propose that mid-replication segregation of sister Ori via enhanced Ori compaction is a general strategy employed by all bacteria in fast-growth conditions. A commonly observed phenomenon in bacteria is the accumulation of parS sites near the Ori [8, 46], which is responsible for Ori compaction via the interplay of ParB and SMC. The proposed mechanistic strategy of Ori segregation could be an evolutionary pressure driving the

clustering of parS sequences near the Ori. For bacteria, like *E. coli*, that lack the ParAB system, the same mechanism is likely driven by a concerted activity of other proteins like MatP and MukBEF [43–45]. Our work emphasizes the need to investigate bacterial proteins that enhance Ori compaction as a driver of chromosome segregation.

Overall, we used data-driven modeling to obtain the polymer structures of the bacterial chromosome (Fig. 1). We then predict the sister-chromosome-resolved Hi-C maps and the chromosomes' structural ensembles at various replication stages (Fig. 2). Analyzing the ensembles, we find that maintaining the compact polymer organization of the Ori-proximal DNA is crucial for the ParAB-driven poleward forces to pull the two replicated Ori to the opposite poles (Fig. 3). We argue that a mechanism combining compaction-mediated segregation with polar pulling forces underlies the rapid and faithful Ori segregation in fast-growing bacteria (Fig. 4). The proposed mechanism is likely a general bacterial strategy for Ori segregation and consolidates a paradigm where genome structure governs function.

Acknowledgements. We thank the National Science Foundation (Grants No. PHY-2019745, No. PHY-2210291, and No. PHY-2014141) and the Welch Foundation (Grant No. C-1792) for funding. We gratefully acknowledge the Center for Research Computing (CRC) at Rice University for providing computational resources for this work. We also thank Advanced Micro Devices for donating critical hardware and support resources from its HPC Fund that contributed to this work.

[1] A. Badrinarayanan, T. B. Le, and M. T. Laub, Bacterial chromosome organization and segregation., Annu Rev Cell Dev Biol. **31**, 171 (2015).
[2] C. Gogou, A. Japaridze, and C. Dekker, Mechanisms for chromosome segregation in bacteria, Frontiers in Microbiology **12** (2021).
[3] A. S. B. Jalal and T. B. K. Le, Bacterial chromosome segregation by the ParABS system., Open Biology **10** (2020).
[4] S. Gruber and J. Errington, Recruitment of condensin to replication origin regions by parb/spooj promotes chromosome segregation in b. subtilis, Cell **137**, 685 (2009).
[5] N. L. Sullivan, K. A. Marquis, and D. Z. Rudner, Recruitment of smc by parb-pars organizes the origin region and promotes efficient chromosome segregation., Cell **137**, 697–707 (2009).
[6] S. Gruber, J.-W. Veening, J. Bach, M. Blettinger, M. Bramkamp, and J. Errington, Interlinked sister chromosomes arise in the absence of condensin during fast replication in b.subtilis, Current Biology **24**, 293 (2014).
[7] X. Wang, O. W. Tang, E. P. Riley, and D. Z. Rudner, The smc condensin complex is required for origin segregation in bacillus subtilis, Current Biology **24**, 287 (2014).
[8] J. Livny, Y. Yamaichi, and M. K. Waldor, Distribution of centromere-like parS sites in bacteria: insights from comparative genomics., J Bacteriol. **189**, 8693 (2007).
[9] H. C. Lim, I. V. Surovtsev, B. G. Beltran, F. Huang, J. Bewersdorf, and C. Jacobs-Wagner, Evidence for a dna-relay mechanism in parabs-mediated chromosome segregation, ELife **3**, e02758 (2014).
[10] A. G. Vecchiarelli, K. C. Neuman, and K. Mizuuchi, A propagating atpase gradient drives transport of surface-confined cellular cargo, Proceedings of the National Academy of Sciences **111**, 4880 (2014).
[11] A. L. Gall, D. I. Cattoni, A. Cournac, A. Koh, J.-B. Fiche, J. Mozziconacci, H. Murray, R. Koszul, and M. Nollmann, Condensin- and replication-mediated bacterial chromosome folding and origin condensation revealed by hi-c and super-resolution imaging., Molecular Cell **59**, 588 (2015).
[12] A. Le Gall, D. Cattoni, B. Guilhas, C. Mathieu-Demazière, L. Oudjedi, J. B. Fiche, J. Rech, S. Abrahamsson, H. Murray, J. Y. Bouet, and M. Nollmann, Bacterial partition complexes segregate within the volume of the nucleoid., Nat. Comm. **7** (2016).
[13] E. Alipour and J. F. Marko, Self-organization of domain structures by dna-loop-extruding enzymes., Nucleic Acids Res. **40**, 11202 (2012).
[14] X. Wang, T. B. Le, B. R. Lajoie, J. Dekker, M. Laub, and D. Z. Rudner, Condensin promotes the juxtaposition of dna flanking its loading site in bacillus subtilis., Genes Dev. **29**, 1661 (2015).
[15] X. Wang, H. B. Brandão, T. B. K. Le, M. T. Laub, and D. Z. Rudner, Bacillus subtilis smc complexes juxtapose chromosome arms as they travel from origin to terminus, Science **355**, 524 (2017).
[16] M. Ganji, I. A. Shaltiel, S. Bisht, E. Kim, A. Kalichava, C. H. Haering, and C. Dekker, Real-time imaging of dna loop extrusion by condensin, Science **360**, 102 (2018).
[17] H. B. Brandão, Z. Ren, X. Karaboja, L. A. Mirny, and X. Wang, Dna-loop-extruding smc complexes can traverse one another in vivo., Nat Struct Mol Biol **28**, 642 (2021).
[18] A. Anchimiuk, V. S. Lioy, F. P. Bock, A. Minnen, F. Boccard, and S. Gruber, A low smc flux avoids collisions and facilitates chromosome organization in *Bacillus subtilis*, ELife **10**, e65467 (2021).
[19] A. B. Oliveira Junior, M. F. Mello, R. J. Oliveira, E. Dodero-Rojas, S. Brahmachari, V. Contessoto, and J. N. Onuchic, A versatile full inversion model reveals high-fidelity features in chromosome organization, to be submitted (2024).
[20] T. B. K. Le, M. V. Imakaev, L. A. Mirny, and M. T. Laub, High-resolution mapping of the spatial organization of a bacterial chromosome, Science **342**, 731 (2013).
[21] S. Tripathi, S. Brahmachari, J. N. Onuchic, and H. Levine, DNA supercoiling-mediated collective behavior of co-transcribing RNA polymerases, Nucleic Acids Research **50**, 1269 (2021).
[22] E. Kim, A. M. Gonzalez, B. Pradhan, J. van der Torre, and C. Dekker, Condensin-driven loop extrusion on supercoiled dna., Nat Struct Mol Biol **29**, 719 (2022).
[23] C. Dekker, C. H. Haering, J.-M. Peters, and B. D. Rowland, How do molecular motors fold the genome?, Science

382, 646 (2023).

[24] N. El Najjar, D. Geisel, F. Schmidt, S. Dersch, B. Mayer, R. Hartmann, B. Eckhardt, P. Lenz, and P. L. Graumann, Chromosome segregation in bacillus subtilis follows an overall pattern of linear movement and is highly robust against cell cycle perturbations., mSphere **5**, e00255 (2020).

[25] C. W. Shebelut, J. M. Guberman, S. van Teeffelen, A. A. Yakhnina, and Z. Gitai, ¡i¿caulobacter¡/i¿ chromosome segregation is an ordered multistep process, Proceedings of the National Academy of Sciences **107**, 14194 (2010).

[26] S. Brahmachari, T. Markovich, F. C. MacKintosh, and J. N. Onuchic, Temporally correlated active forces drive chromosome structure and dynamics, bioRxiv (2023).

[27] A. Goloborodko, M. V. Imakaev, J. F. Marko, and L. Mirny, Compaction and segregation of sister chromatids via active loop extrusion, eLife **5**, e14864 (2016).

[28] S. Brahmachari and J. F. Marko, Chromosome disentanglement driven via optimal compaction of loop-extruded brush structures, Proceedings of the National Academy of Sciences **116**, 24956 (2019).

[29] S. Brahmachari, V. G. Contessoto, M. Di Pierro, and J. N. Onuchic, Shaping the genome via lengthwise compaction, phase separation, and lamina adhesion, Nucleic Acids Research **50**, 4258 (2022).

[30] S. Mangiameli, B. Veit, H. Merrikh, and P. Wiggins, The replisomes remain spatially proximal throughout the cell cycle in bacteria., PLoS Genet. **13**, e1006582 (2017).

[31] P. H. Viollier, M. Thanbichler, P. T. McGrath, L. West, M. Meewan, H. H. McAdams, and L. Shapiro, Rapid and sequential movement of individual chromosomal loci to specific subcellular locations during bacterial dna replication, Proceedings of the National Academy of Sciences **101**, 9257 (2004).

[32] E. Helgesen, F. Satre, and K. Skarstad, Topoisomerase iv tracks behind the replication fork and the seqa complex during dna replication in escherichia coli., Sci Rep **11** (2021).

[33] J. Snedeker, M. Wooten, and X. Chen, The inherent asymmetry of dna replication., Annual review of cell and developmental biology **33**, 291–318 (2017).

[34] J. Collier, H. H. McAdams, and L. Shapiro, A dna methylation ratchet governs progression through a bacterial cell cycle, Proceedings of the National Academy of Sciences **104**, 17111 (2007).

[35] L. Babl, G. Giacomelli, B. Ramm, A.-K. Gelmroth, M. Bramkamp, and P. Schwille, Ctp-controlled liquid–liquid phase separation of parb, Journal of Molecular Biology **434**, 167401 (2022).

[36] S. Jun and B. Mulder, Entropy-driven spatial organization of highly confined polymers: Lessons for the bacterial chromosome, Proceedings of the National Academy of Sciences **103**, 12388 (2006).

[37] A. Lesne, J. Riposo, P. Roger, A. Cournac, and J. Mozziconacci, 3d genome reconstruction from chromosomal contacts., Nat Methods **11**, 1141 (2014).

[38] J. Paulsen, M. Sekelja, A. R. Oldenburg, A. Barateau, N. Briand, E. Delbarre, A. Shah, A. L. Sørensen, C. Vigouroux, B. Buendia, and P. Collas, Chrom3d: three-dimensional genome modeling from hi-c and nuclear lamin-genome contacts., Genome Biol **18**, https://doi.org/10.1186/s13059-016-1146-2 (2017).

[39] B. Zhang and P. G. Wolynes, Topology, structures, and energy landscapes of human chromosomes, Proceedings of the National Academy of Sciences **112**, 6062 (2015).

[40] M. D. Pierro, B. Zhang, E. L. Aiden, P. G. Wolynes, and J. N. Onuchic, Transferable model for chromosome architecture, Proceedings of the National Academy of Sciences **113**, 12168 (2016).

[41] J. Harju, M. van Teeseling, and C. Broedersz, Loop-extruders alter bacterial chromosome topology to direct entropic forces for segregation., Nat Commun **15** (2024).

[42] A. Wasim, A. Gupta, and J. Mondal, A Hi–C data-integrated model elucidates E. coli chromosome's multiscale organization at various replication stages, Nucleic Acids Research **49**, 3077 (2021).

[43] J. Mäkelä and D. Sherratt, Organization of the escherichia coli chromosome by a mukbef axial core., Mol Cell. **78**, 250 (2020).

[44] M. Seba, F. Boccard, and S. Duigou, Activity of mukbef for chromosome management in *E. coli* and its inhibition by matp, eLife **12**, RP91185 (2024).

[45] A. Badrinarayanan, C. Lesterlin, R. Reyes-Lamothe, and D. Sherratt, The Escherichia coli SMC complex, MukBEF, shapes nucleoid organization independently of DNA replication., Journal of bacteriology **194**, 4669–4676 (2012).

[46] Q. Lamy-Besnier, A. Bignaud, J. R. Garneau, M. Titecat, D. E. Conti, A. V. Strempel, M. Monot, B. Stecher, R. Koszul, L. Debarbieux, and M. Marbouty, Chromosome folding and prophage activation reveal specific genomic architecture for intestinal bacteria., Microbiome **11**, 10.1186/s40168-023-01541-x (2023).

[47] K. Klenin and J. Langowski, Computation of writhe in modeling of supercoiled dna, Biopolymers **54**, 307 (2000).

[48] S. C. Weber, A. J. Spakowitz, and J. A. Theriot, Bacterial chromosomal loci move subdiffusively through a viscoelastic cytoplasm, Phys. Rev. Lett. **104**, 238102 (2010).

[49] A. B. O. Junior, V. G. Contessoto, M. F. Mello, and J. N. Onuchic, A scalable computational approach for simulating complexes of multiple chromosomes, Journal of molecular biology **433**, 10.1016/J.JMB.2020.10.034 (2021).

[50] P. Eastman, J. Swails, J. D. Chodera, R. T. McGibbon, Y. Zhao, K. A. Beauchamp, L.-P. Wang, A. C. Simmonett, M. P. Harrigan, C. D. Stern, R. P. Wiewiora, B. R. Brooks, and V. S. Pande., Openmm 7: Rapid development of high performance algorithms for molecular dynamics., PLOS Comp. Biol. **13**, e1005659 (2017).

[51] S. C. Weber, A. J. Spakowitz, and J. A. Theriot, Nonthermal atp-dependent fluctuations contribute to the in vivo motion of chromosomal loci, Proceedings of the National Academy of Sciences **109**, 7338 (2012).

[52] H. A. Shaban, R. Barth, L. Recoules, and K. Bystricky, Hi-d: Nanoscale mapping of nuclear dynamics in single living cells, Genome Biology **21**, 1 (2020).

[53] E. T. Jaynes, Information theory and statistical mechanics, Phys. Rev. **106**, 620 (1957).

[54] J. Messelink, M. van Teeseling, J. Janssen, M. Thanbichler, and C. P. Broedersz, Learning the distribution of single-cell chromosome conformations in bacteria reveals emergent order across genomic scales., Nat Commun **12**, https://doi.org/10.1038/s41467-021-22189-x (2021).

[55] F. Morcos, A. Pagnani, B. Lunt, A. Bertolino, D. S. Marks, C. Sander, R. Zecchina, J. N. Onuchic, T. Hwa, and M. Weigt, Direct-coupling analysis of residue coevolution captures native contacts across many protein families, Proceedings of the

National Academy of Sciences **108**, E1293 (2011), https://www.pnas.org/doi/pdf/10.1073/pnas.1111471108.
[56] T. Mora, A. M. Walczak, W. Bialek, and C. G. Callan, Maximum entropy models for antibody diversity., Proc. Natl Acad. Sci. USA **107**, 5405–5410 (2010).
[57] D. De Martino, A. MC Andersson, T. Bergmiller, C. C. Guet, and G. Tkačik, Statistical mechanics for metabolic networks during steady state growth., Nat. Commun. **9**, https://doi.org/10.1038/s41467-018-05417-9 (2018).
[58] D. P. Kingma and J. Ba, Adam: A method for stochastic optimization, (2017), arXiv:1412.6980.

SUPPLEMENTARY TEXT

S-I. Dynamics simulations using polymer potential

We utilize Langevin dynamics of coarse-grained monomers using the OpenMiChroM software package [19, 49], where the velocity components temporally evolve according to the following equation:

$$m\frac{dv_i}{dt} + m\gamma v_i = -(\nabla U)_i + R_i, \tag{1}$$

where the mass of each monomer is m, the velocity component is v_i, and the friction coefficient is γ (Table I). The thermal noise, given by R_i, has zero mean and is temporally uncorrelated: $\langle R_i \rangle = 0$ and $\langle R_i(t)R_i(t')\rangle = 2m\gamma k_B T\delta(t-t')$, where k_BT sets the scale for thermal energy with T denoting the temperature. The velocity components are integrated via the leap-frog method with a time step $dt = 0.01\tau$, using the OpenMM simulation engine [50]. The term $-\nabla U$ is the force derived from the chromosome potential, written as follows.

$$U = U_{\rm HP} + U_{\rm conf} + U_{\rm ParAB} + U^{\rm ME}_{\rm Hi-C}, \tag{2}$$

where the terms on the R.H.S. are the contributions from, respectively, the homopolymer backbone, the cellular confinement, the ParAB-mediated Ori pulling, and the data-driven pairwise interaction term learned from Hi-C data.

$$U_{\rm HP} = U_{\rm nn} + U_{\rm angles} + U_{\rm sa} \tag{3}$$

The homopolymer term, $U_{\rm HP}$, is a sum of contributions from the nearest neighbor bonding interactions U_{nn}, the three-body angular potential term $U_{\rm angles}$ that gives local stiffness to the polymer, and the soft self-avoidance between all the monomers $U_{\rm sa}$. These three terms are given as follows:

$$U_{\rm nn} = \frac{k_b}{2}\left[\sum_{i=1}^{N-1}(|\vec{r}_i - \vec{r}_{i+1}| - r_b)^2 + (|\vec{r}_1 - \vec{r}_N| - r_b)^2\right] \tag{4}$$

The nearest neighbor interactions are like harmonic springs with an equilibrium distance r_b and bond stiffness k_b (Table I, Fig. S10A). Note that the second term within the brackets corresponds to the circularization of the chromosome polymer.

$$U_{\rm angles} = k_a\left[\sum_{i=2}^{N-1}(1-\cos(\theta_i - \theta_0)) + (1-\cos(\theta_N - \theta_0)) + (1-\cos(\theta_1 - \theta_0))\right] \tag{5}$$

The angle potential constrains the angle between three consecutive monomers to an equilibrium value θ_0 with a stiffness k_a. This angle controls the distance between the next-nearest neighbors (Fig. S10B). We computed the average contact probability between the next-nearest neighbors from the experimental Hi-C map [14], which is then converted into a distance using the definition of a contact (Eq. (11)). This distance is then used to compute the equilibrium angle θ_0 (Table I).

The self-avoidance potential is a soft-repulsive sigmoid where the repulsion is experienced for pairwise distances below $r_{\rm cut}$ (Fig. S10A).

$$U_{\rm sa} = \frac{E_{\rm cut}}{2}\left[\sum_{i=1}^{N}\sum_{j=1}^{N}(1-\delta_{ij})\left(1+\tanh\left(\frac{r_{\rm cut} - |\vec{r}_i - \vec{r}_j|}{r_{sa}}\right)\right)\right] \tag{6}$$

This potential only acts for non-bonded monomers, signified by the Kronecker delta function. The slope of the sigmoid is controlled by the parameter r_{sa}, and the maximum strength of the self-avoidance is given by $E_{\rm cut}$ (Table I).

The confinement potential $U_{\rm conf}$ mimics the effect of confinement by the cell wall. Our model system *B. subtilis* is rod-shaped cells hence we implement a cylindrical confinement potential. We use a flat-bottom potential with a confinement radius of $r_{\rm conf}$(Table I) and the cylindrical axis aligned along the z-axis (Fig. S10C-D). The confinement cylinder is centered at the origin and extends to $\pm z_{\rm conf}$ along the cylindrical z-axis, as follows:

$$U_{\rm conf} = \frac{k_{\rm conf}}{2}\left[\sum_{i=1}^{N}(r_i^{xy} - r_{\rm conf})^2\Theta(r_i^{xy} - r_{\rm conf}) + (z_i - z_{\rm conf})^2\Theta(z_i^2 - z_{\rm conf}^2)\right], \tag{7}$$

where $r_i^{xy} = \sqrt{x_i^2 + y_i^2}$ is the cylindrically symmetric radius, $k_{\rm conf}$ (Table I)is the stiffness of the confinement potential, and the Heavyside-theta function with usual definition shown below ensures the flat-bottom part of the potential.

$$\Theta(x) = \begin{cases} 0 & \text{for } x \leq 0 \\ 1 & \text{for } x > 0 \end{cases} \tag{8}$$

The ParAB potential is given by a double-well potential with exponential decay about the two minima at $\pm z_0$ along the cylindrical axis with the decay rate controlled by w_z, as captured by the function below.

$$U_{\rm ParAB} = \sum_{i\in{\rm parS}}\left[\exp\left(-\frac{|z_i - z_0|}{w_z}\right) + \exp\left(-\frac{|z_i + z_0|}{w_z}\right)\right] \tag{9}$$

The potential is an external, radially symmetric potential with the force only executed for the eight Ori-proximal monomers containing the parS sites (monomers with indices: 5, 17, 45, 371, 398, 399, 400, 403) and is zero for all other monomers (Fig. S10C). When using the replicated chromosome, we add parS sites to the corresponding beads in the sister chromosomes.

Finally, the potential $U_{\rm Hi-C}^{\rm ME}$ is derived from the pairwise constraints of the Hi-C data, as described in the next section (Sec. S-II). We use all the potentials defined above as the reference on top of which $U_{\rm Hi-C}^{\rm ME}$ is learned to recapitulate the experimental Hi-C maps in simulation ensembles.

a. Simulation and physics units

The simulation unit of distance is σ, the coarse-grained monomer size. Each monomer contains 10 kb DNA, and using $\sigma = 80$ nm agrees well with imaging experiments (Fig. 1H-I). The energy scale is set by the thermal temperature T. We defined a reduced temperature $T = 1.0$, which sets the unit of energy $\epsilon = k_BT = 4.21 \times 10^{-21}$ Joules. The unit of mass is set to 1.0.

The simulation unit of time is τ. Using Einstein's relation within the simulation setup, we get $D_{\rm sim} = \epsilon/m\gamma = 10\sigma^2/\tau$, where we used $\gamma = 0.1/\tau$ (see Table I) and the dimensional argument $\epsilon = m\sigma^2/\tau^2$. Now, we compare this diffusion constant with the apparent diffusion constant of a monomer inside a polymer and a free bead to get the bounds of τ. For a polymer: $D_{\rm polymer} = k_BT/\zeta$, where $\zeta \approx 6\pi\eta\sigma N^\nu$ is the effective drag of a monomer. Note, the factor N^ν is the enhancement in drag due to polymer connectivity, where $\nu = 1$ for a Rouse chain and $\nu \approx 0.5$ for an ideal chain with a hydrodynamic radius (Zimm model). Equating the simulation diffusion constant with that of a Rouse chain, and using a typical polymer size $N = 100$, the viscosity of water $\eta = 0.001$ Pa-s, and the above-mentioned values of σ and k_BT, we get $\tau = 1$ sec. While comparing the simulation bead with a free bead ($N = 1$) in water, we get an underestimate $\tau = 0.01$ sec. Comparing with experiments, $\tau = 0.3$ sec gives a reasonable fit with the experimental MSD curves in the time window of few seconds to few minutes, given $\sigma = 80$ nm (Fig. S11). Hence, we use $\tau \approx 0.1$ sec as the typical time conversion. This gives an apparent diffusion constant $D_{\rm sim} \approx 10^{-2}$ μm^2/s, which is within an order or magnitude of experimentally observed values [51, 52]. We simply use the viscosity of water without any known good estimate of nucleoplasm viscosity.

b. Initialization and simulation statistics

We initialized the polymer configuration as a random walk and then equilibrated under the chromosome potential (Eq. 2) for $10^6\tau$ before storing data for calculations. We ran 10 independent replicates with each replicate run spanning $2 \times 10^6\tau$. The simulations used a time step of $dt = 0.01\tau$ and the structures were sampled every 200 steps, giving a total of 10^6 structures per replicate run. All the structures from the replicates were combined to do the statistical analyses and computation of simulated Hi-C maps.

Parameter	Value	Units
γ	0.1	$1/\tau$
k_BT	1.0	ϵ
k_b	30.0	ϵ/σ^2
r_b	1.0	σ
k_a	2.0	ϵ
θ_0	2.03	radians
$E_{\rm cut}$	4.0	ϵ
$r_{\rm cut}$	0.5	σ
r_{sa}	0.2	σ
$k_{\rm conf}$	5.0	ϵ/σ^2
$r_{\rm conf}$	3.0	σ
$z_{\rm conf}$	8.0	σ
w_z	1.0	σ
μ	5.0	$1/\sigma$
r_c	1.5	σ

TABLE I. Parameters used in the simulations and the optimization routine. These parameters were used for the plots in Fig. S10.

c. *Constructing the partially replicated chromosome polymer*

To create the geometry of a partially replicated chromosome, we add a sister chromosome segment to a circular chromosome by harmonically bonding the two extremities of the sister chromosome to the two monomers representing the replication fork positions on the two chromosome arms. Except for the Hi-C derived potential $U^{\rm ME}_{\rm Hi-C}$, all the other potentials are the same as in the non-replicating case. The Hi-C learned potential is constructed according to the scheme described in Fig. 2A.

S-II. Optimizing the chromosome potential from Hi-C data using entropy maximization

We seek to find the potential $U^{\rm ME}_{\rm Hi-C}$, such that a polymer equilibrated under the total potential U (Eq. (2)) recapitulates the experimental Hi-C map of bacteria *B. subtilis* [14]. The problem may be cast as a search for a probability distribution such that samples from the distribution give chromosome structures consistent with the Hi-C maps. We build upon a statistical mechanical approach of entropy maximization, originally proposed by E.T. Jaynes [53] and later implemented in various forms for chromosome structures [19, 39, 40, 54], protein structures [55], and other kinds of biophysical data [56, 57]. We implement the technique developed in Ref. [19] for optimizing the potential $U^{\rm ME}_{\rm Hi-C}$.

Assuming the bacterial chromosome is a circular homopolymer in the presence of the ParAB and confinement potentials, the most general potential consistent with the maximum-entropy approach gives

$$U^{\rm ME}_{\rm Hi-C}(\vec{r},\vec{\lambda}) = \sum_i \sum_{j>i} \lambda_{ij}\phi_{ij}(r_{ij}), \tag{10}$$

The coefficients λ_{ij} are the Lagrange multipliers associated with the contact probability between the monomer pairs i and j, denoted by ϕ_{ij}. We define a contact using a sigmoidal function as follows:

$$\phi_{ij} = \frac{1}{2}\left(1+\tanh\left[\mu(r_c - r_{ij})\right]\right), \tag{11}$$

where, $r_{ij} = |\vec{r}_i - \vec{r}_j|$ and μ, r_c are hyperparameters (Table I). This approach of defining a contact within a simulated structure to recapitulate Hi-C contact has been used before [39, 40].

The average contact probability that is compared with the experimental values is computed from the simulated structures, and can be represented as follows:

$$\langle\phi_{ij}\rangle = \frac{1}{\mathcal{Z}}\int \mathcal{D}\psi(\vec{r})\ \phi_{ij}\ \exp(-\beta U[\psi(\vec{r})]), \tag{12}$$

where $\mathcal{D}\psi(\vec{r})$ denotes the integration over various structures of the polymer ensemble, U is the total chromosome potential (Eq. (2)) that is a functional of the polymer configuration, and the normalization factor is given by the partition function:

$$\mathcal{Z} = \int \mathcal{D}\psi(\vec{r}) \ \exp(-\beta U[\psi(\vec{r})]). \tag{13}$$

Our goal is to find all the λ_{ij} values such that the contact probabilities obtained from the Hi-C experiments $\phi_{ij}^{\exp}$ are equal to the simulated contact probabilities $\langle\phi_{ij}\rangle$. We use an iterative scheme to obtain λ_{ij} where the iterative updates are derived from the gradient of an objective function (Fig. 1B). We defined a convex objective function as:

$$\Theta(\vec{\lambda}) = \ln \mathcal{Z}(\vec{\lambda}) + \sum_{ij} \lambda_{ij}\phi_{ij}^{\exp}, \tag{14}$$

such that the gradient is given by

$$g_{ij} \equiv \frac{\partial\Theta}{\partial\lambda_{ij}} = \langle\phi_{ij}\rangle - \phi_{ij}^{\exp}. \tag{15}$$

The iterative updates to the Lagrange multipliers are computed using an adaptive gradient method called Adam [58], where the second-order derivatives of the objective function are estimated from the first-order derivatives. The update formula used in this work is obtained from Algorithm 1 of Ref. [58]:

$$\lambda_{ij}(t) = \lambda_{ij}(t-1) - \frac{\alpha\hat{m}_{ij}(t)}{\sqrt{\hat{v}_{ij}(t)} + \varepsilon}, \tag{16}$$

where $\hat{m}_{ij}(t) = m_{ij}(t)/(1-\beta_1^t)$ and $\hat{v}_{ij}(t) = v_{ij}(t)/(1-\beta_2^t)$, and the corresponding updates are given by: $m_{ij}(t) = \beta_1 m_{ij}(t-1)+(1-\beta_1)g_{ij}(t)$ and $v_{ij}(t) = \beta_2 v_{ij}(t-1)+(1-\beta_2)g_{ij}^2(t)$. Here, $\beta_1 = 0.9$, and $\beta_2 = 0.999$ are hyperparameters set according to Ref. [58], and we used a learning rate $\alpha = 0.02$. The details of the optimization over iterations and the optimized Lagrange multipliers λ_{ij} are shown in Figs. S1, S2, and S3.

a. *Preprocessing experimental Hi-C maps*

We need to recalibrate the experimental contact probability to our polymer simulations. This is necessary because the experimental probabilities must be adjusted to ensure that the probability of contact between the nearest neighbors, a bonded interaction in our simulations, is 1.0. The experimental Hi-C maps obtained from Ref. [14] were normalized probability matrices, such that the sum along each row and column is 1.0. However, the self contact (diagonal) and the nearest neighbor contact (first diagonal parallel to the main diagonal) terms are set to zero (Fig. S12A). We use the contact probability between the origin monomer (0°) and its left neighbor as the probability of the nearest neighbor contact. Within our simulations, the probability of being in contact with the nearest neighbor is 1.0. Hence, we renormalize probabilities by the nearest neighbor value, such that the first parallel diagonal has all values equal to 1.0. We use an additional step of smoothing the Hi-C data with a median filter of window 3 to remove intense single pixels, which is at odds with our polymer hypothesis (Fig. S12B). Further, we shift the experimental matrices to put the Origin at the center of the map for better presentation (Fig. S12C). All the maps in the main figures are with the Ori at the center.

b. *Polymer simulations and enhanced sampling*

Polymer simulations were performed during each iteration of optimization using the updated force fields λ_{ij}. Instead of running multiple replicas, we ran one long simulation to save computational cost. We tempered the polymer every $2\times10^6\tau$ to randomize the initial configurations mimicking a replica. We increased the temperature of the simulation to 3.3 then gradually reduced it in steps of 0.25 to 1.0, while equilibrating in the new temperature for $10^5\tau$. After returning to the normal simulation temperature of 1.0, the simulations were run for an additional time of $10^5\tau$ before collecting data for analyzing the ensembles. This tempering allowed us to sample the polymer configurations better.

S-III. Analysis of simulation trajectories

a. *Simulated Hi-C maps*

The pairwise distances computed for each structure in an ensemble were converted to probabilities using the definition of a simulated Hi-C contact ϕ_{ij} (Eq. (11)). The average ϕ_{ij} matrix is the simulated Hi-C map.

Experimental data	Reference	Source
WT Hi-C	Wang et al. (2015) [14]	GEO accession: GSM1671399
ΔParAB Hi-C	Wang et al. (2015) [14]	GEO accession: GSM1671401
ΔSMC Hi-C	Wang et al. (2015) [14]	GEO accession: GSM1671414
Imaging $\pm 87^\circ$ loci	Wang et al. (2015) [14]	Fig. 1C
Imaging $-64^\circ/-125^\circ$ loci	Wang et al. (2015) [14]	Fig. 1D
Imaging inter-Ori distance	El Najjar et al. (2020) [24]	Fig. 6

TABLE II. Sources for experimental data used in this paper. All the data were accessed on Dec 25, 2023.

b. Inter-sister entanglements

The catenations between the sister chromosomes are computed using the Gauss double integral over the two sister chromosome curves S_1 and S_2 [47]:

$$\mathrm{Ca} = \frac{1}{4\pi} \int_{S1} \int_{S2} \frac{(d\vec{r}_1 \times d\vec{r}_2) \cdot \vec{r}_{12}}{r_{12}^3} \tag{17}$$

where $\vec{r}_1$ and $\vec{r}_2$ are bond vectors along the two sister chromosome curves. Since catenations are defined for closed curves, we joined the monomers preceding the replisome monomer with a straight segment to close the contour for the two sister chromosomes (Fig. S6). Following the approach in "Method 1a" of Ref. [47], we use the geometric interpretation of the cross-product to compute the integral.

S-IV. Experimental data

We have used Hi-C matrices provided by Ref. [14] from the Gene Expression Omnibus (GEO) repositories (see Table II). We have quantified curves from figures in Refs. [14] and [24] that correspond to imaging data (see Table II).

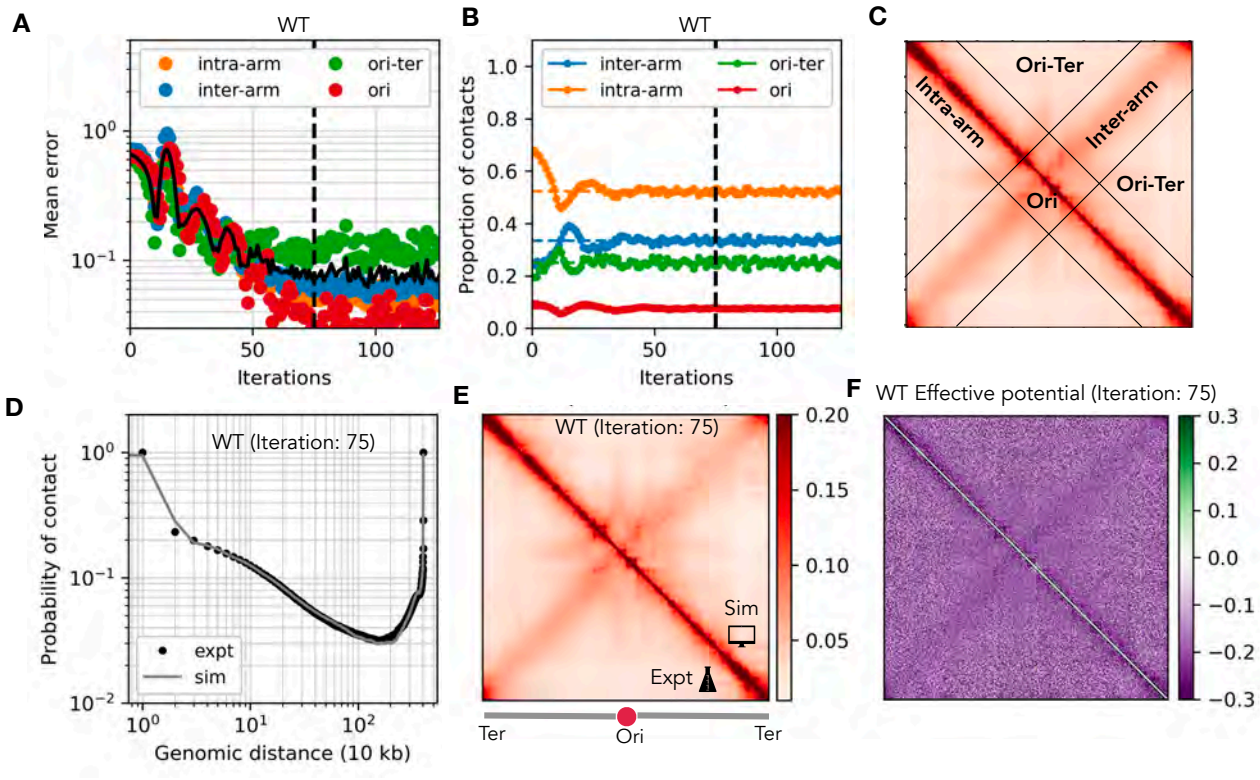

FIG. S1. **Optimization of chromosome structures from WT Hi-C data.** The Optimization scheme fits a polymer potential to the experimental WT Hi-C map of *B. subtilis* (Fig. 1B) [14]. Between iteration steps, polymer dynamics simulations generate structural ensembles that are used to generate the simulated contact map. The polymer is confined in a cylinder with the ParAB double-well potential. (A) Mean error over the optimization iterations. Mean Error is calculated from the average of the absolute difference between the simulated contact maps and WT Hi-C experiment[14]. We use iteration 75 (dashed vertical line) as the effective potential for WT. (B) Hi-C components over iterations. The components are calculated from the simulated contact maps, as shown in (C). (D) WT simulated pairwise-contact probability scaling with genomic distance (line), compared with experiments (dots) [14]. (E) WT simulated contact map (upper triangle) compared with experiments [14] (lower triangle). The Ori is at the center. (F) WT effective potential. The interactions are predominantly attractive (purple) except for weak repulsion at the semiflexibility length of a few monomers, represented as positive potential (green) near the diagonal.

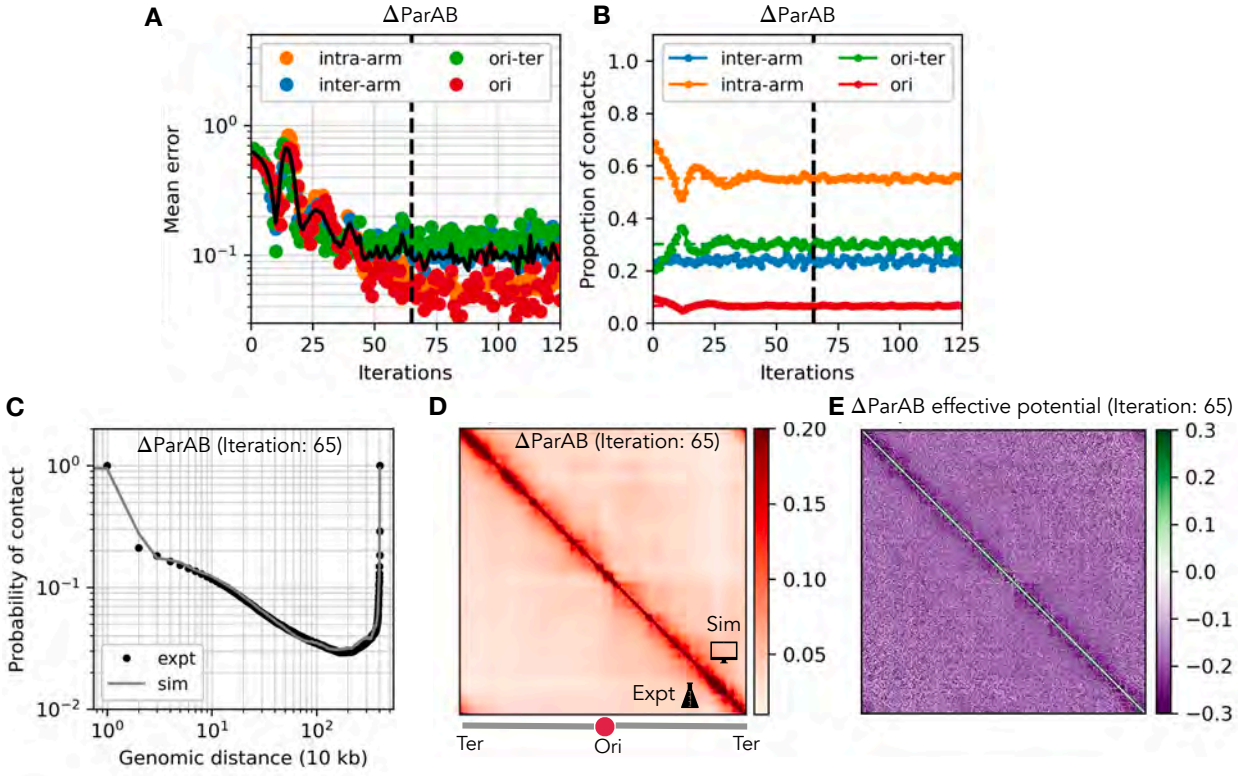

FIG. S2. **Optimization of chromosome structures from ΔParAB Hi-C data.** Compare with Fig. S1. ΔParAB optimized potential lacks the attractive interactions between loci pair equidistant from the Ori seen in WT.

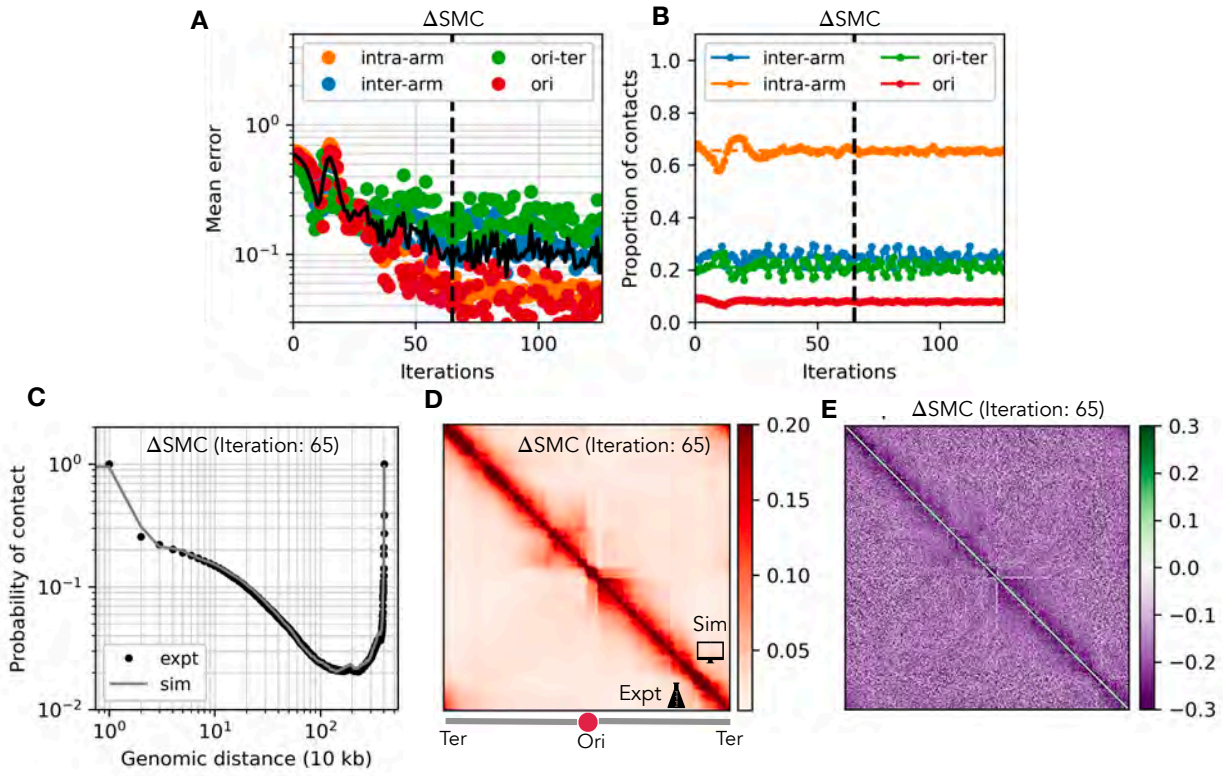

FIG. S3. **Optimization of chromosome structures from ΔSMC Hi-C data.** Compare with Fig. S1. ΔSMC optimized potential lacks the attractive interactions between loci pair equidistant from the Ori seen in WT, contact map antidiagonal is absent. ΔSMC potential shows more attractive interactions between genomic neighbors, resulting in a thicker diagonal in the contact map and the effective potential.

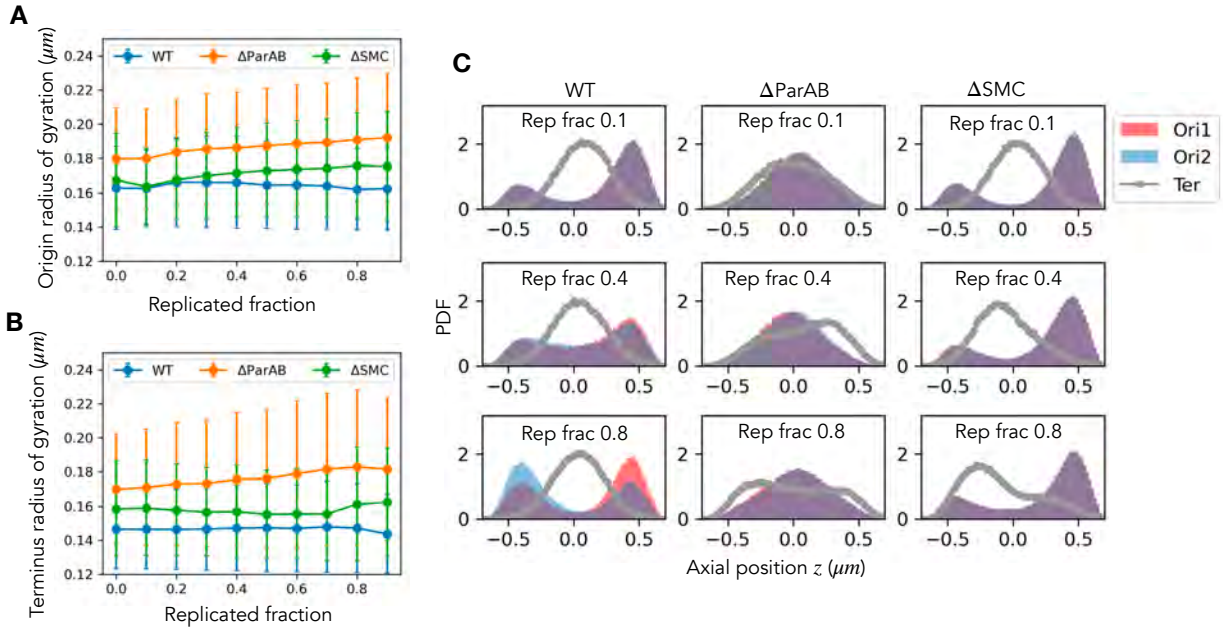

FIG. S4. **Axial localization and compaction of Ori and Ter regions.** (A) Radius of gyration of the Ori-proximal region (40-bead segment centered at the Ori). The Ori is more compact for WT, which underlies the inter-Ori repulsion. (B) Radius of gyration of the Terminus regions (40-bead segment centered at the Ter) shows a more compact Ter in WT. (C) Axial positions of the two Ori and the Ter regions for various replication fractions are shown in the rows, while the WT, ΔParAB, and ΔSMC ensembles are shown in columns. The WT and ΔSMC ensembles show polar Ori localization, whereas, the ΔParAB ensemble shows a mid-cell positioning of the two Ori. The terminus is located mid-cell for WT in all stages of replication. ΔParAB ensemble shows a mid-cell Terminus that moves towards the poles during later replication stages.

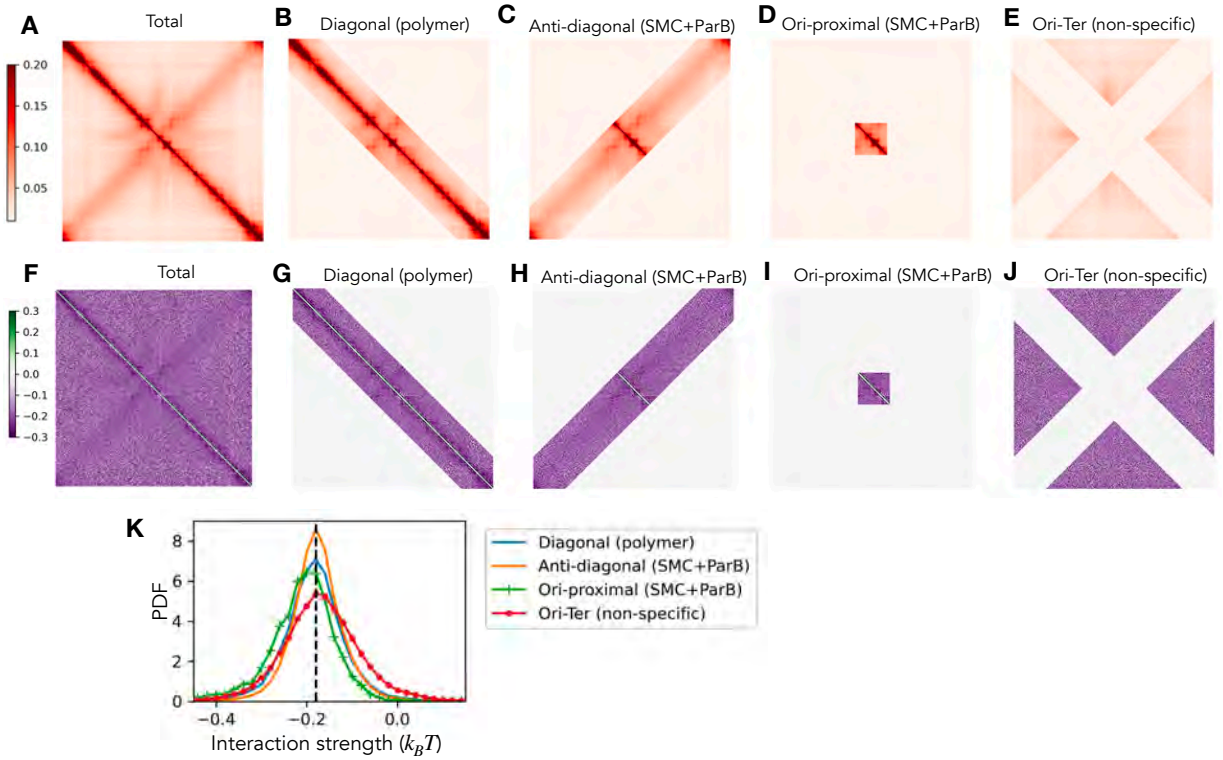

FIG. S5. **Components of Hi-C map and effective potential.** (A) WT Hi-C map [14] with Ori positioned at the center of the map. (B) The "diagonal" contribution to the Hi-C interactions, which are dominated by the polymer nature of the chromosome. (C) The "anti-diagonal" contribution is driven mainly by the SMC/ParB activity of pairing the arms. (D) Hi-C contribution from the Ori-proximal region which is driven by a combination of polymer nature and the SMC/ParB activity. (E) The residual interactions after taking out the contributions from the SMC/ParB and polymer nature are considered non-specific interactions. These non-specific interactions populate the Ori-Ter contacts. (F) The effective learned potential for the WT map. The various contributions to the potential are shown in (G)-(J). (K) The probability density of the effective potential or interaction strengths (in k_BT units) for the various contributions. Higher compaction of the Ori-proximal regions leads to a skew of the Ori-proximal contribution to more negative values. The dashed vertical line (-0.18 k_BT) corresponds to the average non-specific interaction strength that is used for uniform inter-sister interactions for the replicating chromosome potential (Fig. 2A).

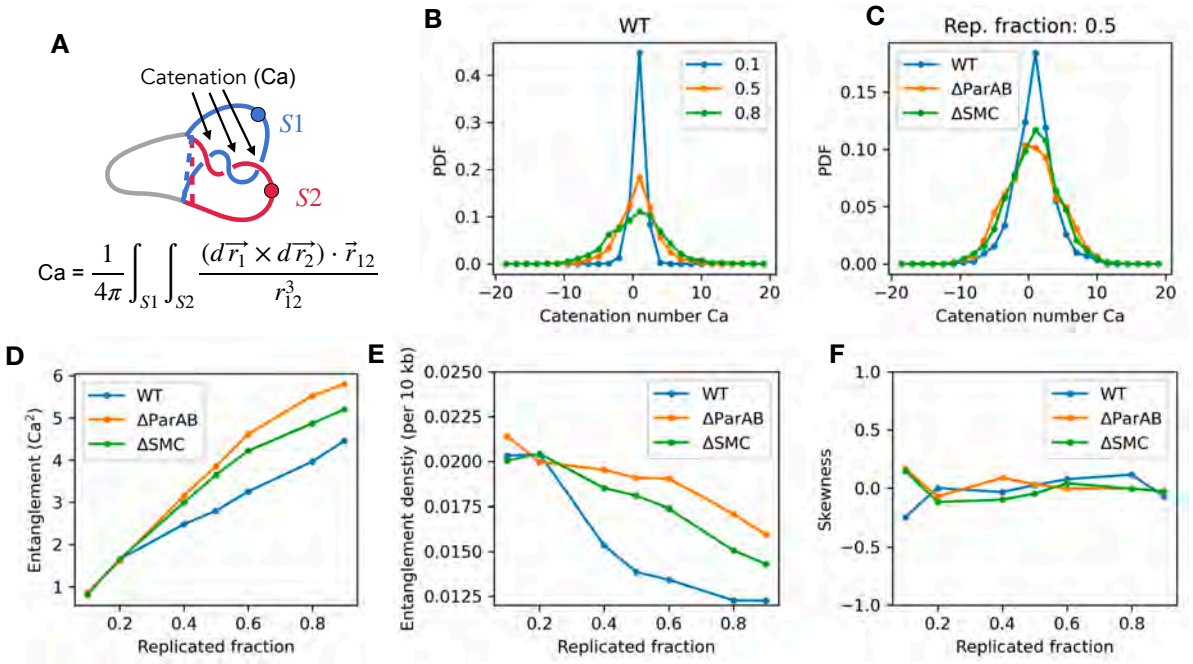

FIG. S6. **Inter-sister catenation or entanglement.** (A) Schematic showing the catenations between the sister chromosomes. The definition of catenation or Ca is written as a Guass double integral over the two sister chromosomes [47]. Since catenation is only defined for closed curves, we join the two sisters near the replication fork using a straight connecting line to produce two closed curves for the two sisters and then compute their catenation, using the "Method 1a" in Ref. [47] that takes a geometrical approach to computing the double integral. (B) The distributions of catenation calculated for various structures in the WT ensemble corresponding to the replicated fractions 0.1, 0.5, and 0.8. (C) Catenation distribution for the WT and mutant ensembles for a replicated fraction of 0.5. Note that the distributions are symmetric about zero because the structural ensembles have equilibrated topology. In such an ensemble with fluctuating polymer topology, the width of the catenation distribution is a measure of entanglement. An ensemble will exhibit a higher proportion of catenated or entangled structures when the catenation distribution is broader. Thus, an efficient mechanism of disentanglement in a fluctuating topology ensemble is to reduce the width of the catenation distribution, which may be achieved via physical segregation. (D) Entanglement or the width of the catenation distribution, i.e., $\langle Ca^2 \rangle$ is plotted for various replication fractions for the WT and mutants. The structures indicate there are about 5 entanglements between the sister chromosomes at 10 kb resolution in mid-replication stages. The WT structures are less entangled than the mutants. (E) Entanglement density, computed by dividing the width of the catenation distribution by the size of the sister chromosomes. This indicates the typical number of catenations stored per 10 kb DNA. The WT ensemble shows a significant decrease in entanglement density with replicated fraction. The y-axis of this plot is renormalized as a fold change over the replication fraction 0.1 and plotted in Fig. 3B. (F) The skewness of the catenation distributions. The distributions are essentially symmetric due to topology fluctuations that make positive and negative catenations equally probable.

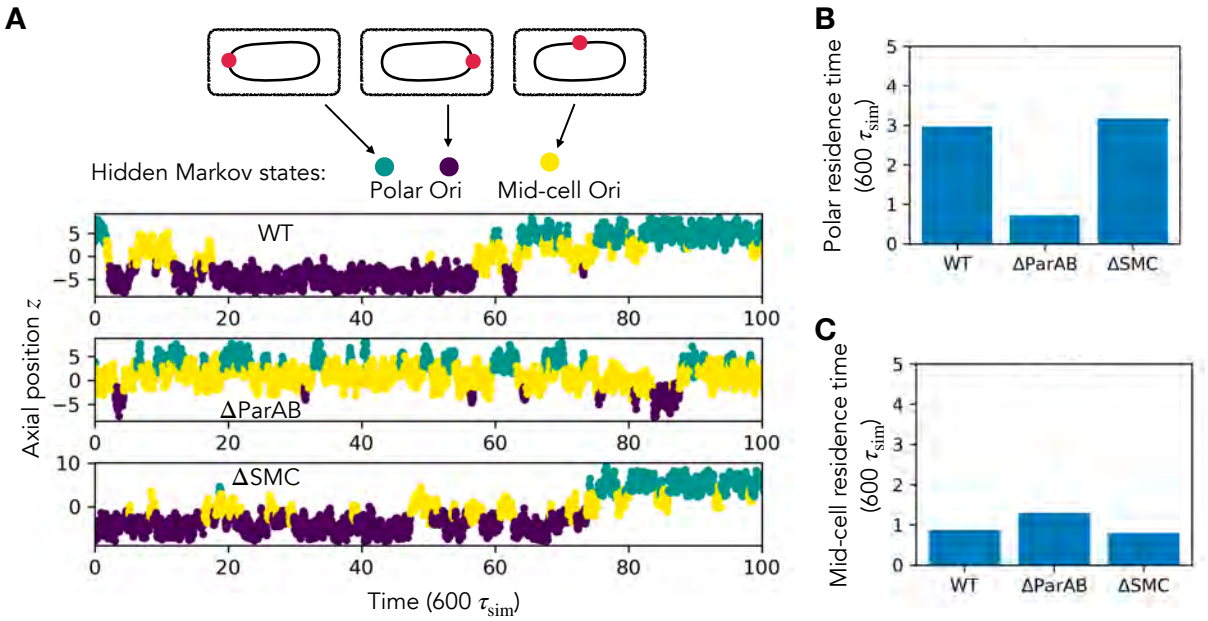

FIG. S7. **Hidden Markov modeling to ascertain Ori dynamics time scales.** (A) Scheme of Hidden Markov modeling. The temporal variation of the axial position of an Ori is fed to a three-state Gaussian hidden Markov model that learns the three Ori states as a mid-cell (yellow) and two polar configurations (purple and green). We obtain the best-fit transition rate matrix and then compute the residence time of the polar state as the inverse of the rate of escaping the polar configuration. Similarly, the residence time of the mid-cell state is computed from the inverse rate of escaping the mid-cell configuration. (B) Polar residence time and (C) Mid-cell residence time for the three trajectories of the WT and mutants shown in panel (A).

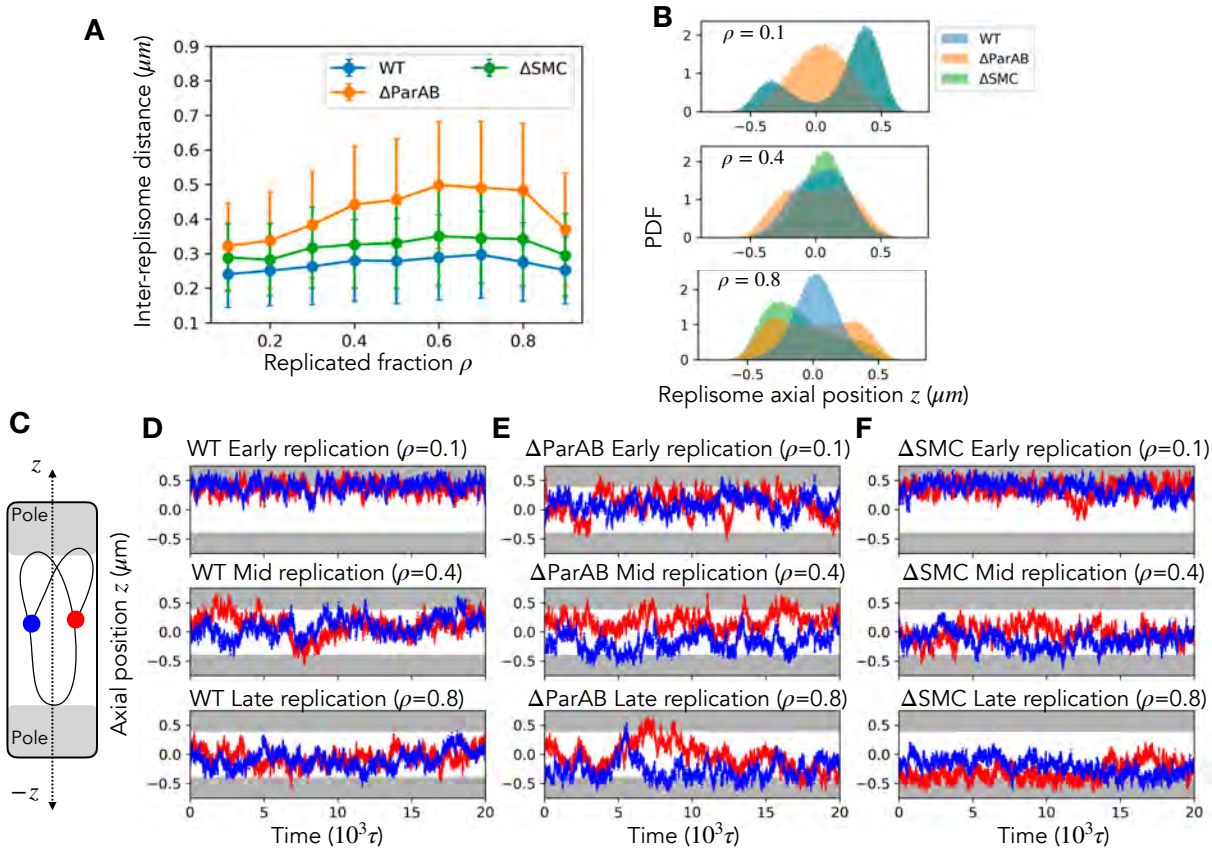

FIG. S8. **Replisome positioning.** (A) Inter-replisome or inter-replication fork distance as a function of the replication fraction. WT ensemble shows the most proximal replisomes compared to the mutants. (B) Axial position of the two replisomes for various replication fractions ρ. In early replication, the WT ensemble shows a polar localization of the replisomes that move to the mid-cell during the mid-replication stage and stay there till the end of the replication cycle. The replisomes in the ΔParAB ensemble start mid-cell during the early stages of replication, and then the two replisomes move toward the opposite poles. In the ΔSMC ensemble, the two replisomes start at the same pole; then they move mid-cell, much like the WT ensemble. However, in the late replication stages, both the replisomes move toward the same pole, with the other pole being occupied by the unsegregated Ori. (C) Schematic of the bacterial cell with the cylindrical axis along z direction and the poles shaded in gray. The two replisomes are depicted as red and blue circles. (D) Axial dynamics of the two replisomes (red and blue) for WT at replication fractions of 0.1 (early replication, top panel), 0.4 (mid-replication, middle panel), and 0.8 (late-replication, bottom panel). The same for the ΔParAB mutant is shown in (E) and the ΔSMC mutant is shown in (F).

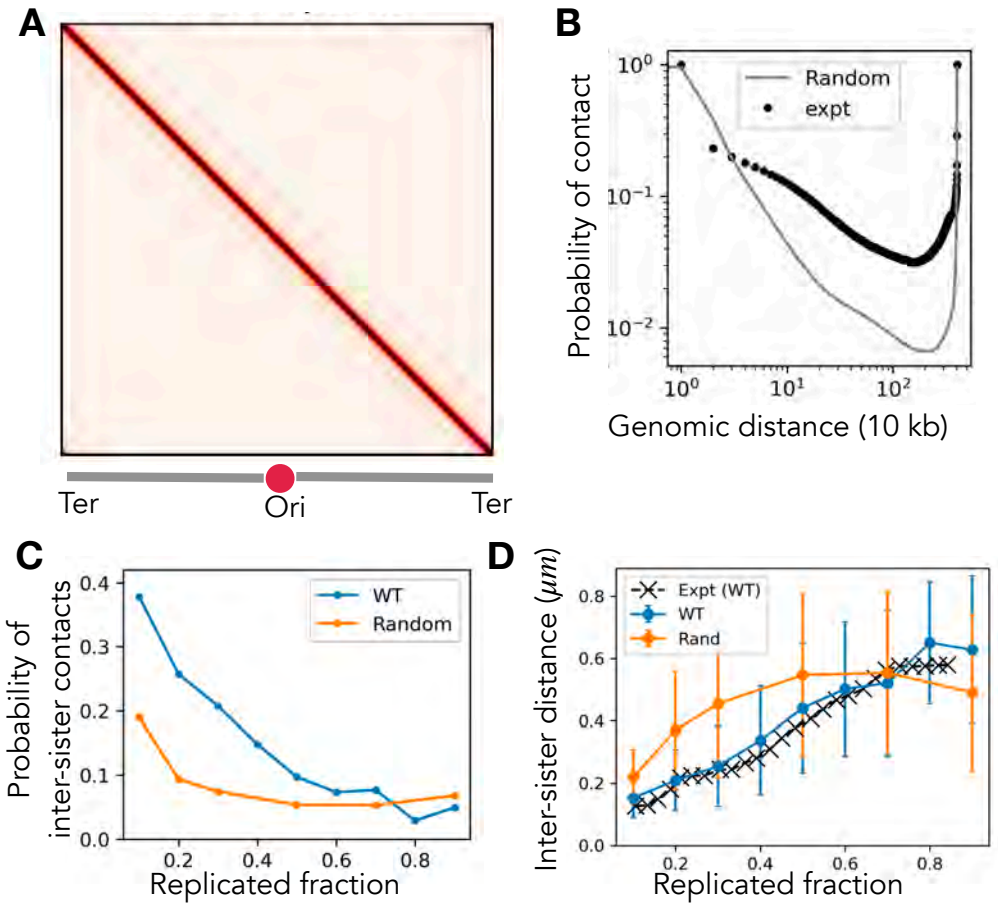

FIG. S9. **Chromosome structure and Ori segregation in cylindrically confined random polymers.** (A) Hi-C map of a random circular polymer. The only contributions to the random polymer potential come from the polymer connections and the self-avoidance interactions. (B) The probability of pairwise contact between the monomers of the simulated random polymer is shown by the solid line. The experiments are shown by points [14] (Fig. 1D). (C) Average probability of inter-sister contacts as a function of replication fraction, compared between the simulations with the learned WT potential and the random polymer potential. (D) Average distance between the centers of masses of the Ori-proximal regions of the two sister chromosomes as a function of the replicated fraction. The random polymer shows an efficient segregation between the sister chromosomes at the early stages of the replication cycle. This results from the purely self-avoiding, repulsive interactions between the monomers. Although there is segregation of the sister chromosomes, the random-polymer structures are not representative of the experimental data for bacteria [14].

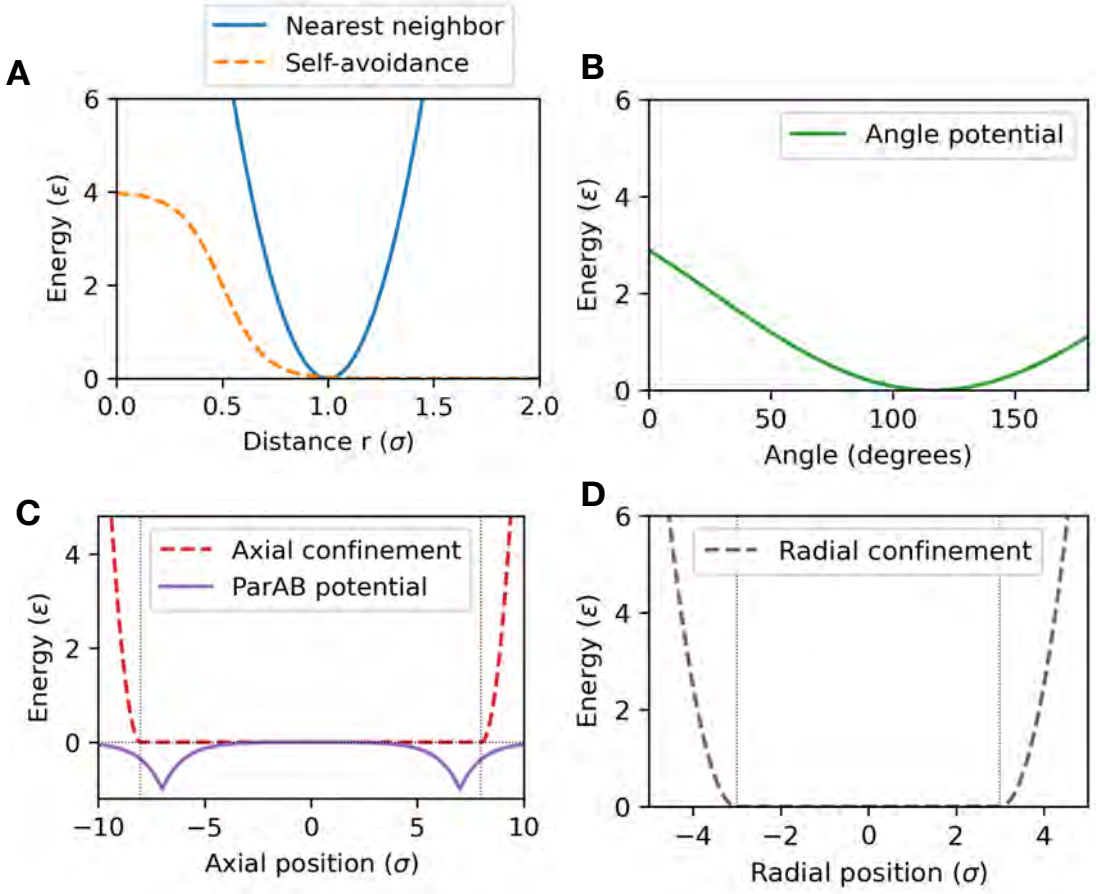

FIG. S10. **Simulation potentials.** (A) The nearest neighbor bonding potential [Eq. (4)] and the non-bonding self-avoiding potential [Eq. (6)] between the non-neighboring monomers are shown as a function of inter-monomer distance. The bonding term has a minimum at the distance 1.0σ, which sets the bond length. The self-avoidance term kicks in for distances below 1.0σ signifying repulsion from monomer overlap. (B) The potential constraining the three-body angles, i.e., the angles between the monomers i, $i+1$, and $i+2$ [Eq. (5)]. The minimum is at 116° which is set such that the distance between the next-nearest neighbors corresponds to the experimental scenario. (C) The confinement [Eq. (7)] and ParAB [Eq. (9)] potentials as a function of the axial position. The confinement potential restrains the monomer axial position within the confinement dimension $\pm 8\sigma$. The ParAB potential has minima near the two poles at $\pm 7\sigma$. (D) The confinement potential [Eq. (7)] as a function of the radial position, showing confinement within a cylindrical radius of 3σ.

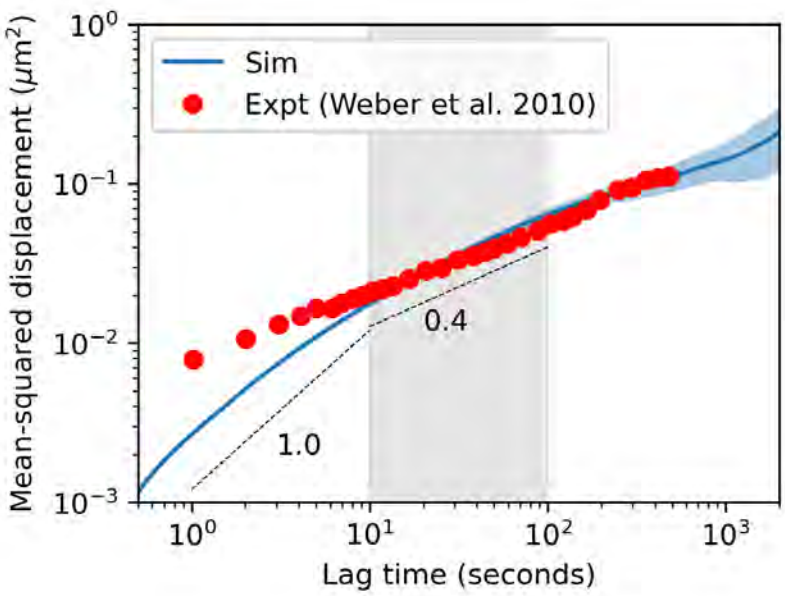

FIG. S11. **Comparison of simulation and experimental dynamics.** Mean-squared displacement (MSD) $\langle |r_n(t+\Delta t) - r_n(t)|^2 \rangle$ is plotted versus lag time Δt. The red circles are experiments on *Escherichia coli* from Ref. [48]. The solid line is *B. subtilis* simulations using $\sigma = 80$ nm and $\tau = 0.3$ seconds. The scaling of both the MSD curves is about 0.4 in the time window of 10-100 sec, suggesting sub-diffusive motion of bacterial loci at a few seconds to a few minutes time scale. Note that the experiments represent 2D MSD, and the MSD obtained from 3D simulations is adjusted (multiplied by 2/3) to compare with experiments.

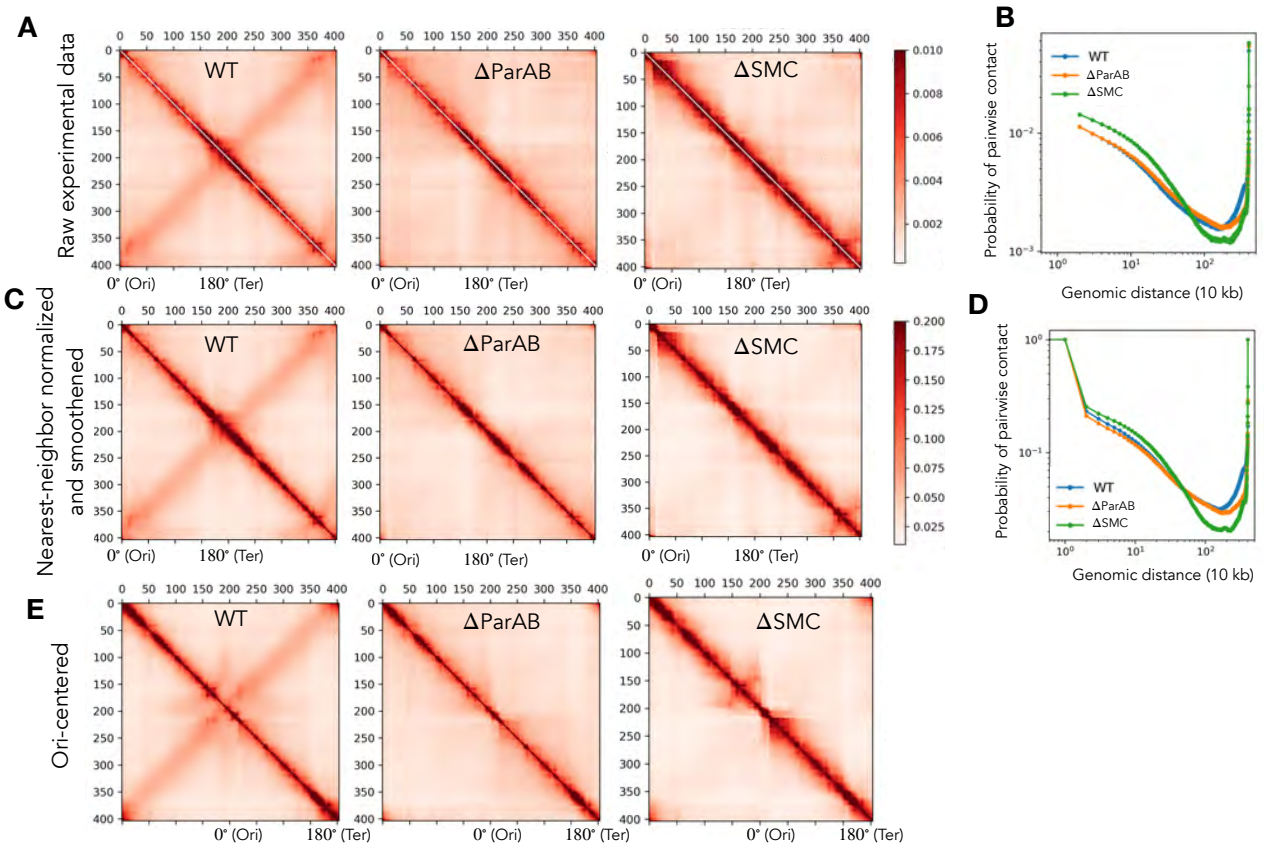

FIG. S12. **Preprocessing Hi-C data.** (A) Raw experimental Hi-C matrices as obtained from Ref. [14]. Note the missing values for the diagonal and the nearest-neighbor contacts. The Ter region (180°) is centered in these maps. (B) Probability of contact versus genomic distance for the raw Hi-C map. (C) Normalized and smoothed Hi-C matrices. We select the contact between the farthest points as the nearest neighbor value since the polymer is a ring. We then normalize all the probabilities by the nearest neighbor value such that the probability of nearest-neighbor contact is 1.0. The probability of self-contact, i.e., the main diagonal is also set to 1.0. We then smooth the map using a median filter of window size 3 to remove high-intensity dots. Note that the smoothing does not have any significant impact on the Hi-C maps or the optimization procedure. (D) Probability of contact versus genomic distance for the nearest-neighbor normalized and smoothed Hi-C map. (E) The processed Hi-C maps are shifted to put the Ori at the center of the map.